Climate variability in a 3.8 Ma old sedimentary record from the hyperarid Atacama Desert

Felix L. Arens [a,*], Jenny Feige [a,b], Alessandro Airo [a,b], Christof Sager [a,b], Lutz Hecht [b], Lucas Horstmann [c,d], Felix E.D. Kaufmann [b], Johannes Lachner [e,f], Thomas Neumann [g], Norbert Nowaczyk [q], Ferry Schiperski [g], Peter Steier [e], Alexandra Stoll [h,i], Ulrich Struck [b], Bernardita Valenzuela [j], Friedhelm von Blanckenburg [k,l], Hella Wittmann [k], Lukas Wacker [m], Dirk Wagner [c,n], Pedro Zamorano [o], Dirk Schulze-Makuch [a,c,p]

[a] Technische Universität Berlin, Zentrum für Astronomie und Astrophysik, 10623 Berlin, Germany
[b] Museum für Naturkunde, Leibniz-Institut für Evolutions- und Biodiversitätsforschung, 10115 Berlin, Germany
[c] GFZ German Research Centre for Geosciences, Section Geomicrobiology, 14473 Potsdam, Germany
[d] Department Experimental Phycology and Culture Collection of Algae (EPSAG), Albrecht-von-Haller-Institute for Plant Sciences, Georg August University Göttingen, 37073 Göttingen, Germany
[e] University of Vienna, Faculty of Physics, Isotope Physics, 1090 Vienna, Austria
[f] Helmholtz-Zentrum Dresden-Rossendorf (HZDR), Institute of Ion Beam Physics and Materials Research, 01328 Dresden, Germany
[g] Technische Universität Berlin, Institut für Angewandte Geowissenschaften, Fachgebiet Angewandte Geochemie, 10623 Berlin, Germany
[h] Laboratorio de Microbiología Aplicada, Centro de Estudios Avanzados en Zonas Áridas, La Serena 1720256, Chile,
[i] Instituto de Investigación Multidisciplinario en Ciencia y Tecnología, Universidad de La Serena, La Serena 1720256, Chile
[j] Laboratorio de Microorganismos Extremófilos, Instituto Antofagasta, Universidad de Antofagasta, Antofagasta 1240000, Chile,
[k] GFZ German Research Centre for Geosciences, Section Earth Surface Geochemistry, Telegrafenberg, 14473 Potsdam, Germany
[l] Fachbereich Geowissenschaften, Freie Universität Berlin, 12249 Berlin, Germany
[m] Ion Beam Physics, ETH Zürich, 8093 Zürich, Switzerland
[n] University of Potsdam, Institute of Geosciences, 14476 Potsdam, Germany
[o] Departamento Biomédico, Facultad de Ciencias de la Salud, Universidad de Antofagasta; Antofagasta 1240000, Chile
[p] Department of Plankton and Microbial Ecology, Leibniz Institute of Freshwater Ecology and Inland Fisheries, 16775 Stechlin, Germany
[q] GFZ German Research Centre for Geosciences, Section Paleoclimate and Landscape Evolution, 14473 Potsdam, Germany

ARTICLE INFO

ABSTRACT

The hyperarid Atacama Desert is one of the driest and oldest deserts on Earth, rendering it a valuable climate archive. However, unraveling its past climate is particularly challenging and the few studied paleoclimate records of the region reveal strong temporal and spatial variabilities. To enhance our understanding of these dynamics we investigated a sedimentary record in the Yungay valley located in the southern hyperarid Atacama Desert. We employed paleomagnetic and radiocarbon dating, and for the first time for Atacama Desert sediments, a meteoric ^{10}Be/^{9}Be based method for determining the depositional age. The respective 4.20 m deep profile comprises a lower alluvial fan deposit with a maximum age of 3.8 ± 0.8 Ma, and an upper 1.84 m thick clay pan deposit that has accumulated over the last 19 ka. Different proxies including grain size, salt concentration, and elemental composition indicate an aridity increase around 2.3 Ma ago and repeated dry and wet phases during the late Pleistocene and the Holocene. The latter climatic shifts can be assigned to variabilities of the South American Summer Monsoon and El Niño Southern Oscillation with moisture sources from the Atlantic and the Pacific Ocean, respectively. This study provides deeper insights into the heterogeneous climate of the hyperarid Atacama Desert and underlines the importance of interdisciplinary investigations to decipher climate systems and their effect on potential habitable regions in such an extreme environment.

---

1. Introduction

The temperate Atacama Desert, Chile, is one of the most arid deserts on Earth and has persisted since the late Triassic (Clarke, 2006). The onset of hyperaridity occurred between the late Oligocene and early Miocene (e.g., Dunai et al., 2005; Evenstar et al., 2017). Furthermore, evidence has been found that since then multiple periods of increased precipitation interrupted the hyperaridity (e.g., Jordan et al., 2014; Ritter et al., 2018a). However, these punctuations occurred rather locally (Ritter et al., 2018b). Despite the overall hyperarid conditions,

very rare but heavy rain events can cause flash floods and result in the temporary flooding of closed drainage systems, creating clay pans (a.k.a. playas) (Amundson et al., 2012; Pfeiffer et al., 2018; Ritter et al., 2018a, 2019; Diederich et al., 2020; Wennrich et al., 2024) (Fig. 1). There are numerous basins located in the Coastal Cordillera that incorporate clay pans (10^2–10^3 m in diameter), with deposition records spanning 10s–100s ka and high sedimentation rates of 10s of m Ma^{-1}, compared to the millions of years old surrounding alluvial fans with much slower sedimentation rates of ~1 m Ma^{-1} (Jungers et al., 2013; Ritter et al., 2019; Diederich et al., 2020; Wennrich et al., 2024). Moreover, their
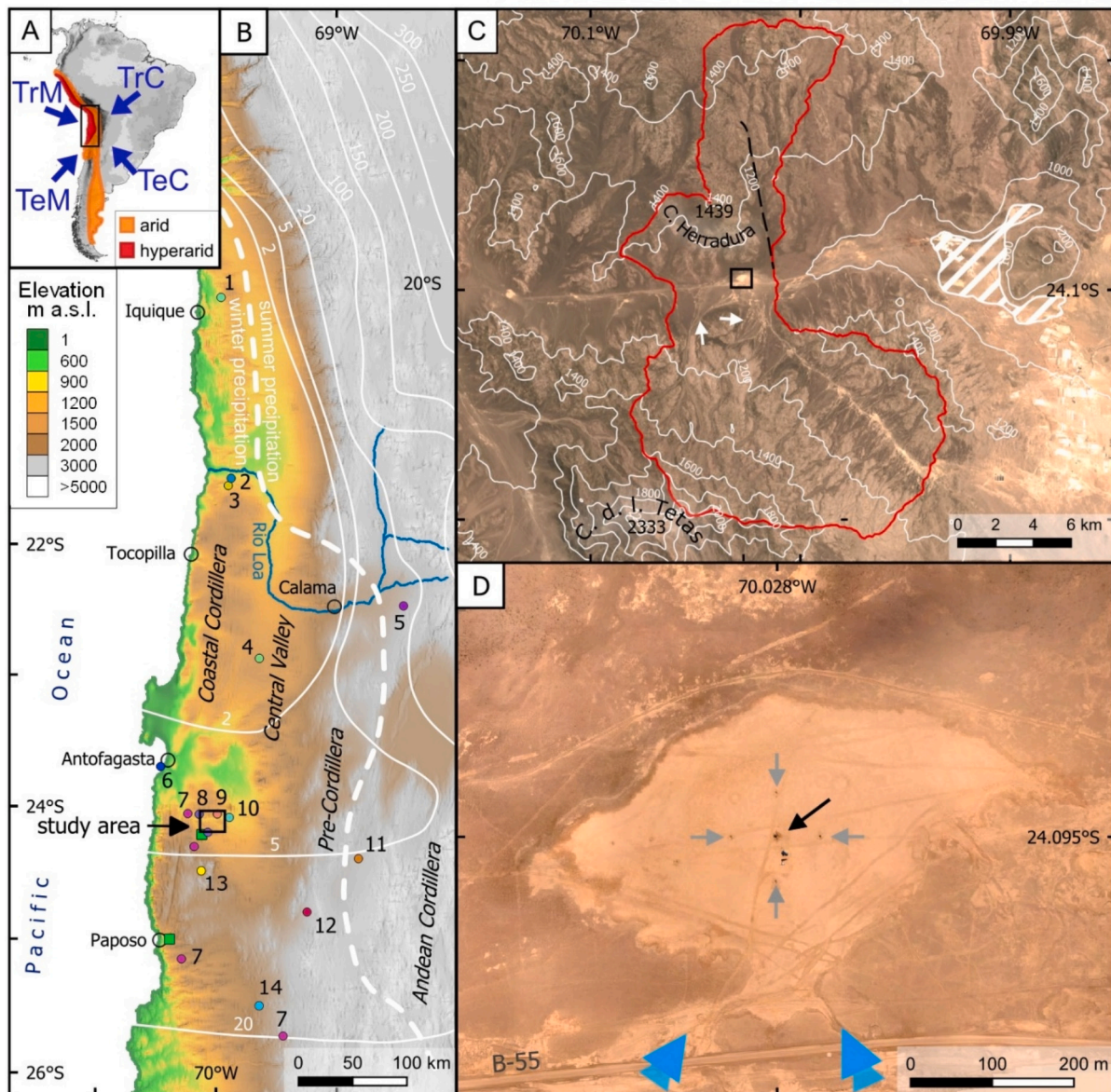

Fig. 1. Overview maps of the study area. A) South America with arid and hyperarid climate zones (Houston and Hartley, 2003) and the main moisture sources (blue arrows) relevant for the Atacama Desert: tropical continental (TrC), temperate continental (TeC), tropical maritime (TrM), temperate maritime (TeM) (Houston and Latorre, 2022). Black rectangle shows zoom-in of B. B) The topographic map of the Atacama Desert with the mean annual precipitation (mm a^{-1}) is shown as isohyets (white lines) after Ritter et al. (2019) and the border of the summer- and winter-precipitation dominated areas (white dashed line) after Houston (2006b). Location of recent Huidobria fruticosa shrubs (green rectangle) and location of paleo records discussed in this study (dots) (1. Diederich et al., 2020; 2. Ritter et al., 2018b; 3. Ritter et al., 2019; 4. Wang et al., 2015; 5. González-Pinilla et al., 2021; 6. Vargas et al., 2006; 7. Diaz et al., 2012; 8. Placzek et al., 2014; 9. Amundson et al., 2012; 10. Pfeiffer et al., 2018; 11. Quade et al., 2008; 12. Sáez et al., 2016; 13. Wennrich et al., 2024; 14. Maldonado et al., 2005) Black rectangle shows zoom-in of C. C) Landsat-8 satellite image with 200 m contour lines (white lines) of the Yungay valley and the investigated clay pan, here referred to as the 'Herradura' clay pan (black rectangle, showing zoom-in of D) with its 188 km² large catchment area (red outline), as well as the adjacent Aguas Blancas salar in the east (white line pattern). The black dashed line indicates a fault going through the valley (Domagala et al., 2016). D) Drone orthophoto of the 0.1 km² large Herradura clay pan with the main pit (black arrow) and the four adjacent pits (gray arrows). From the south, recent (2017) run-off channels (blue arrows) have introduced new sediment into the clay pan, also flooding the road B-55. (For interpretation of the references to colour in this figure legend, the reader is referred to the web version of this article.)

catchment areas are hydrologically disconnected from the Andes and therefore hold records of these local environments within the hyperarid core of the Atacama Desert (Diederich et al., 2020). Hence, they provide an opportunity to gain a more comprehensive picture of the climatic and ecological evolution within the Atacama Desert and to understand the regional variabilities (e.g., Amundson et al., 2012; Sáez et al., 2016; Ritter et al., 2019; Diederich et al., 2020; Wennrich et al., 2024) (Fig. 1B). These paleo environmental studies are also important to gain insights into the preservation of biological matter and the former habitability under hyperarid conditions, which can help to understand the environmental conditions and the habitability of Mars (Davila and Schulze-Makuch, 2016; Azua-Bustos et al., 2023).

The younger clay pan deposits can be dated by multiple geochronological methods including magnetostratigraphy, radiocarbon, and optically stimulated luminescence (OSL) dating (Ritter et al., 2019; Diederich et al., 2020). Dating the millions of years old alluvial fan deposits, however, is more challenging, since radiocarbon and OSL are limited to maximal ages of 60 and 350 ka, respectively (e.g., Murray and Olley, 2002; Bartz et al., 2020). Biostratigraphy is also not applicable in the hyperarid core of the Atacama Desert due to the lack of microfossils while magnetostratigraphy is a challenge due to the coarse grain size and the typically discontinuous sedimentation of alluvial deposits. Hence, the depositional ages of these Ma-old sediments are in large parts only constrained by individual marker horizons, such as volcanic ashes or ignimbrites that can be dated with Ar—Ar or U—Pb methods (e.g., Ewing et al., 2006; Rech et al., 2006).

More compelling are dating methods with cosmogenic radionuclides such as ^{10}Be that is produced from secondary cosmic rays reacting with O and N (Lal and Peters, 1967). In-situ produced ^{10}Be forms in the minerals themself and yields exposure ages, that e.g., have been used to constrain the cessation of alluvial activity correlating with the latest onset of hyperaridity ~2 Ma ago (Amundson et al., 2012; Jungers et al., 2013). Depositional ages, however, can be directly determined through meteoric ^{10}Be, which is produced in the Earth's atmosphere (Raisbeck and Yiou, 1984). Its half-life of 1.387 Ma (Chmeleff et al., 2010; Korschinek et al., 2010) allows for depositional age dating within the range of 0.2–14 Ma (Bourles et al., 1989). Thus far, only a single study in the Atacama Desert has used ^{10}Be soil concentrations for incremental time-resolved stratigraphy of alluvial deposits (Wang et al., 2015). However, the depositional process and sediment type, such as changing sedimentation rates, varying grain sizes and compositions, affect the final ^{10}Be concentrations and therefore reduce the accuracy of the depositional ages (Bourles et al., 1989; Wittmann et al., 2012). This inaccuracy can be compensated through the measurement of the stable isotope ^{9}Be deriving from bedrock weathering and using ^{10}Be/^{9}Be ratios for depositional dating (e.g., Bourles et al., 1989). This approach relies on the assumption that ^{10}Be and ^{9}Be have similar depositional mechanisms (Wittmann et al., 2012).

In this study, we deployed a unique set of methods across multiple disciplines, including a novel dating technique of meteoric ^{10}Be/^{9}Be dating for millions of years old soils based on alluvial fans formed under hyperarid conditions, and ^{14}C dating coupled with magnetostratigraphy for the clay pan deposits. Combined with geochemical, sedimentological and phytologic analysis on sediment deposits in the Yungay valley (24°S, 71°W; 1010 m above sea level) a more comprehensive paleo record on the regional climate variability in the Atacama Desert is provided over a million-years range.

2. Regional setting

Numerous factors collectively contribute to the extreme aridity of the Atacama Desert (Houston and Hartley, 2003; Houston, 2006b; Garreaud et al., 2010). Besides its position in the subtropical high-pressure belt, the distance to the Atlantic Ocean as a main moisture source and the rain shadow effect that developed with the orogenesis of the Andean Cordillera increases the aridity (Houston and Hartley, 2003). The cold

Humboldt Current causes further aridification by cooling the above-lying air and thereby reducing its moisture capacity (Garreaud et al., 2010). This process causes a temperature inversion and leads to the formation of persistent stratus cloud cover, which can reach elevations of up to 1200 m above sea level (a.s.l.). In the coastal region, these clouds create fog, providing an important water source for the local vegetation (Houston, 2006b; Cereceda et al., 2008; Latorre et al., 2011). The Coastal Cordillera (<2000 m a.s.l.) is effectively blocking the fog from penetrating further inland, except for a few topographical corridors where it can migrate several kilometers into the desert. The Andean Cordillera, bordering the Atacama Desert in the east, receives mean annual precipitation of 300 mm a^{-1} at 5000 m a.s.l. which decreases with lower elevation to <20 mm a^{-1} at 2300 m a.s.l. In the hyperarid core of the Atacama Desert located between 19°S and 25°S mean annual precipitation can be <1 mm a^{-1} (Houston and Hartley, 2003). Lastly, the high evaporation rates amplify the prevailing dry climate conditions (Houston, 2006a). The main sources of precipitation in the Atacama Desert are from the Atlantic Ocean and the Pacific Ocean, which are influenced by the El Niño Southern Oscillation (ENSO) (Houston, 2006b). The Atlantic moisture occurs as South American Summer Monsoon from the north-northeast (tropical continental) and from the southeast (temperate continental) during the summer and especially during La Niña events (Fig. 1A). The Pacific moisture occurs as extra-tropical cyclones from the southwest (temperate maritime) and tropical precipitation anomalies from west and northwest (tropical maritime) during the winter and especially during El Niño (Houston, 2006b; de Porras et al., 2017). The different proximity of these sources leads to a divide into two regions of summer-dominated precipitation and winter-dominated precipitation, where precipitation is minimal at their boundary (Houston, 2006b; Quade et al., 2008) (Fig. 1B). Records in the Atacama Desert and adjacent Andean Cordillera have shown that these precipitation sources have changed within orbital (i.e., Milankovitch cycles) and millennial timescales throughout the late Pleistocene and Holocene (e.g., Placzek et al., 2009; Sáez et al., 2016; Ritter et al., 2019). This dynamic also influenced the position of the boundary (Houston and Latorre, 2022).

The dominating geomorphological features of the Atacama Desert, i. e., alluvial fans and stream incisions, are mostly formed during more moist, but still arid periods millions of years ago (Amundson et al., 2012; Jordan et al., 2014; Ritter et al., 2018b). In contrast, during the recent stage of hyperaridity depositional processes are reduced around two orders of magnitude with overall sedimentation rates of 0.5–5 m Ma^{-1} (Davis et al., 2014; Sanchez et al., 2021). Moreover, seismic activity became relevant for the net sediment transport on sloped surfaces (Sager et al., 2020), and atmospheric dust and salt accumulation dominated, leading to a soil volume expansion typical for the Atacama Desert (Ericksen, 1981; Michalski et al., 2004; Ewing et al., 2006).

The saline fraction of atmospheric input with a current depositional rate of ~4 g m^{-2} a^{-1} is largely not washed away by flash floods after minor rain events but rather infiltrates differentially into the soil (Ewing et al., 2006; Owen et al., 2013). The most soluble components (e.g., chlorides or nitrates) can migrate downward up to a few meters, whereas the shallow subsurface is dominated by sulfates (Ewing et al., 2006; Ewing et al., 2008; Arens et al., 2021). These soils show a typical stratification beginning with the surficial ~30 cm thick gypsic horizon (locally termed *chusca*) composed of surface clasts lying on loose sand-rich sediment with embedded *losas* (local name for palm-sized, spheroidal aggregates) underlain by the vesicular layer (porous and fragile horizon), both highly concentrated in sulfates. Below lies a multiple meters thick gravelly petrogypsic horizon, firmly cemented by sulfates (*costra*), followed by a petrosalic horizon (*caliche*) recognizable by its high chloride and nitrate content (Ericksen, 1981; Finstad et al., 2014).

2.1. Study area

The investigated clay pan (24.095°S, 70.028°W) is here referred to as

Herradura clay pan named after the adjacent mountain in the north (Fig. 1, S1). The ~0.1 km² large clay pan and its current catchment area of 188 km² is located in the eastern Coastal Cordillera, 60 km southeast of Antofagasta (Fig. 1B). The surrounding mountains are built up by igneous bedrock, reaching over 2300 m a.s.l. and their slopes are covered by alluvial fans which have accumulated atmospheric dust and salts (Amundson et al., 2012; Domagala et al., 2016). The Herradura clay pan is situated at an elevation of 1010 m a.s.l. and is part of in an endorheic basin with its spill point leading into the Aguas Blancas salar (960 m a.s.l.) located ~8 km further east (Fig. 1C). The sedimentary profile was sampled down to 4.20 m in a preexisting pit located in the center of the clay pan. This pit is surrounded by four ~1 m deep pits at 50 m distance, which display the same stratigraphy supporting that the investigated profile represents the overall buildup of the clay pan (Fig. 1D).

3. Methods

3.1. Sampling

The profile samples were taken after laterally excavating the pit by more than 50 cm for collecting pristine samples. In total three different sample sets were taken in two field campaigns in 2018 and 2019: Sample set A was taken in 10 cm increments and a vertical thickness of roughly 5 cm from the surface down to bottom of the pit. Sample set B was taken in a similar manner but regarding the identified sedimentary horizons within the upper 185 cm. Both sets were stored in polyethylene sample bags. Sample set C was collected with cubic plastic boxes (internal size $2.0 \times 2.0 \times 1.6$ cm) at a standard distance (center to center) of 2.5–3.0 cm for the upper 187 cm. For each undisturbed sample cube of set C azimuth, inclination, and rotation were determined with a geological compass. This sampling technique was not applicable for sediments below 187 cm being coarse-grained and salt cemented. All sets were stored at room temperature.

3.2. pH and electrical conductivity (EC)

The pH and EC measurements were conducted in the Astrobiology laboratory of the Technische Universität Berlin. Subsamples (5 g) from sample set A were dried at 60 °C and sieved dry to remove the >2 mm grain size fraction before further analysis. Ultra-pure water was added in 1:2.5 and 1:5 (w/w) ratio to the processed subsamples, respectively, and shaken for 60 min before measuring the pH-value (pH meter 691, Metrohm) and EC (GMH 3400, Greisinger).

3.3. Grain size distribution

The grain size analysis was conducted at the Department of Applied Geochemistry of the Technische Universität Berlin. The non-soluble grain fraction of subsamples from sample set A and B (100 g) was wet sieved with distilled water employing 5 mesh sizes: <0.063 mm (clay and silt); 0.063–0.25 mm (fine sand); 0.25–0.63 mm (medium sand); 0.63–2 mm (coarse sand); >2 mm (pebbles and cobbles). Subsequently, the <0.063 mm fractions were further suspended in water and separated into clay and silt fraction by centrifugation (Heraeus Megafuge 1.0) with settling distance of 10 cm and relative centrifugal force of 210 x*g* for 3 min. Mean grain size, standard deviation, skewness, and kurtosis were calculated with GRADISTAT (Blott and Pye, 2001).

3.4. Mineralogy

For the bulk mineralogy, subsamples from sample set A and B were crushed, homogenized and further ground to powder. X-ray diffraction (XRD) analysis was performed by using a D2 Phaser XRD device (Bruker) at the Department of Applied Geochemistry of the Technische Universität Berlin. The X-ray source is a CuK$_\alpha$ anode operating at 30 kV and

10 mA. A step interval of 0.1° (2Θ) with a step-counting time of 1 s was used in a scanning range from 3° to 80° (2Θ). For clay mineral identification smear slides of the clay fractions were measured in air-dried, ethylene glycol saturated, and 550 °C preheated configuration. A semi-quantitative evaluation of the results was conducted with the software package "Diffrac.eva" (Bruker) and the "Powder Diffraction File Minerals 2019" (File and others, 2000).

3.5. Ion chromatography (IC)

Cation and anion analysis was performed on a SYKAM Compact IC system (Sykam Chromatographie, Fürstenfeldbruck, Germany) at the GFZ German Research Centre for Geosciences, Potsdam. Sample preparation was done according to Genderjahn et al. (2018) with subsamples of set A dried at 50 °C for 12 h and sieved to <2 mm grain size. The leaching was performed in a 1:5 ratio of 5 g soil to 25 mL Milli-Q water and diluted according to their electric conductivity prior to ion chromatographic measurement. Standards for the detection of cations (Roth, Multi-Element IC Standard Solution, covering lithium, sodium, ammonium, potassium, magnesium, and calcium) and anions (Sykam, covering fluoride, chloride, nitrite, bromide, nitrate, phosphate, and sulfate) were used. The samples were run in triplicates to estimate the error based on the standard deviation.

3.6. Micro X-ray fluorescence (µ-XRF)

A vertical profile consisting of single point µ-XRF analyzes every ca. 3 mm was obtained on sample set C with a Bruker Tornado Plus spectrometer at the Museum für Naturkunde Berlin. Single points were measured with an Rh X-ray tube set at 50 kV and 600 µA with an X-ray spot size of 160 µm and a measuring time of 60 s. 10 measurements per sample were averaged to obtain a ~1 cm resolution.

3.7. Concentration and stable isotope analysis of carbon and nitrogen

Subsamples from set A were dried at 60 °C and ground to powder before applying the isotope analysis.

3.7.1. TC, TN, $\delta^{13}C_{TC}$, and $\delta^{15}N_{TN}$

Stable isotope analysis and concentration measurements of total nitrogen (TN) and total carbon (TC) was performed simultaneously with a THERMO/Finnigan MAT V isotope ratio mass spectrometer, coupled to a THERMO Flash EA 1112 elemental analyzer via a THERMO/Finnigan Conflo IV- interface in the stable isotope laboratory of the Museum für Naturkunde Berlin. Stable isotope ratios are expressed in the conventional delta notation ($\delta^{13}C$, $\delta^{15}N$) relative to atmospheric nitrogen (Mariotti, 1983) and Vienna PeeDee Belemnite standard (VPDB). The standard deviation for repeated measurements of lab standard material (peptone) is generally better than 0.15 ‰ for $\delta^{13}C$ and $\delta^{15}N$. Standard deviations of concentration measurements of replicates of our lab standard are <3 % of the concentration analyzed.

3.7.2. $\delta^{18}O_{carbonate}$ and $\delta^{13}C_{carbonate}$

For oxygen and carbon isotope measurements of carbonates approximately 100–400 µg of sample material was put into a clean 10 mL exetainer. After sealing the exetainer with a septum cap (caps and septa for LABCO exetainer 438b) the remaining air was removed by flushing the exetainer with He for 6 min at a flow of 100 mL per minute. After flushing, approximately 30 µL of anhydrous phosphoric acid was injected through the septum into the sealed exetainer by using a disposable syringe. Approximately after 1.5 h of reaction time at 50 °C the sample was ready for isotope measurement. The oxygen and carbon isotopic composition in the CO_2 in the headspace was measured using a Thermo Finnigan GASBENCH II coupled online with a Thermo Finnigan Delta V isotope ratio mass spectrometer. Reference gas was pure CO_2 (4.5) from a cylinder calibrated against the VPDB standard by using

IAEA reference materials (NBS 18, NBS 19). Isotope values are shown in the conventional delta-notation ($\delta^{18}O$, $\delta^{13}C$) in ‰ (VPDB). Reproducibility of replicate measurements of lab standards (limestone) is generally better than 0.10 ‰ (one standard deviation (1 SD)).

3.8. $^{10}Be/^9Be$ ratios

Subsamples (0.5 g) from the sample set A were dried at 105 °C and leached for 6 h using 0.04 M $NH_2OH \cdot HCl$ in 25 % (v/v) acetic acid (Bourles et al., 1989) in the Helmholtz Laboratory for the Geochemistry of Earth Surface (HELGES) at GFZ, Potsdam. This procedure dissolves meteoric ^{10}Be adsorbed onto any particulate matter (i.e., clay particles) without dissolving the (coarse grained) silicate fraction containing in-situ produced ^{10}Be. Samples and processing blanks were prepared further according to Wittmann et al. (2015). An aliquot was taken for the determination of stable natural ^9Be as well as other cations (Al, Ca, Fe, K, Mg, Mn, Na) using ICP-OES. The samples were spiked with 150 μg of ^9Be carrier to determine $(^{10}Be/^9Be)_{carrier}$ ratios using accelerator mass spectrometry (AMS) measurements, after anion and cation exchange chromatography, subsequent alkaline precipitation, oxidation, and mixing with BeO:Nb in a 1:6 weight ratio.

The $(^{10}Be/^9Be)_{carrier}$ AMS ratios were determined at the Vienna Environmental Research Accelerator (VERA) facility of the University of Vienna, Austria, with a method described in Steier et al. (2019). The ratios were measured relative to the Dresden-AMS (DREAMS) standard material SMD-Be-12, with a $^{10}Be/^9Be$ ratio of $(1.704 \pm 0.030) \times 10^{-12}$ (Akhmadaliev et al., 2013). After blank ratio (1×10^{-15} to 4×10^{-14}) subtraction, $(^{10}Be/^9Be)_{carrier}$ were converted into natural $^{10}Be/^9Be$ ratios. Fluxes Φ of ^{10}Be within each sediment layer with thickness Δd and corresponding age interval Δt were calculated with $\Phi(^{10}Be_{dc}) = C(^{10}Be_{dc}) \times \rho \times \Delta d/\Delta t$, where $C(^{10}Be_{dc})$ refers to the ^{10}Be concentration corrected for radioactive decay, and ρ is the estimated layer density of 1.5 g cm^{-3}.

3.9. Seed identification and semi-quantification

The plant seeds were extracted from a subsample of sample set A and B by using their buoyancy in water. After stirring the water sediment mixture thoroughly, the buoyant seeds were picked from the water surface and dried at 60 °C. For comparison seeds from living shrubs were collected close to the catchment area. The recovered seeds were investigated under light microscope and using a JEOL-6610LV scanning electron microscope at the Museum für Naturkunde Berlin for identification. Additionally, seeds from sample set A were counted for semi-quantification.

3.10. ^{14}C dating

Radiocarbon (^{14}C) of the seeds from sample set A and B, the only source of sufficient organic matter in the profile, was measured at the AMS laboratory of the ETH Zürich. The small samples containing only between 10 and 100 μg of carbon were measured on a MICADAS type system equipped with a gas ion source for the direct ^{14}C determination after sample combustion (Ruff et al., 2010; Wacker et al., 2013), avoiding any potential sample contamination due to the laborious step of sample graphitization. The associated calibrated ages were obtained using the software Calib Rev. 8.1.0 (Stuiver and Reimer, 1993) in conjunction with the calibration curve SHCal20 (Hogg et al., 2020).

3.11. Magnetostratigraphy

The paleo and rock magnetic analyses were applied to the samples from set C at the GFZ, Potsdam. The natural remanent magnetization (NRM) was measured and demagnetized with a 2G Enterprises 755 SRM long-core magnetometer with an in-line tri-axial alternating field demagnetizer. An anhysteretic remanent magnetization (ARM) was imparted to discrete samples with a separate 2G Enterprises 600 single-axis alternating field demagnetizer, with an alternating field amplitude of 100 mT and a superimposed static field of 0.05 mT. Measurements and stepwise demagnetization were performed with the long-core magnetometer after applying field amplitudes up to 65 mT in order to determine the median destructive field (MDF), and to provide data for estimation of the relative paleo-intensity (rPI) variations using ARM normalization. The latter was calculated using the NRM/ARM intensity ratio after demagnetization at 30mT each. Low-field magnetic volume susceptibility (κ_{LF}) measurements were performed with an AGICO Kappabridge MFK1-A. The paleomagnetic methods and results are described in more detail in the supplements as well as their results (Fig. S2, S3). The calibrated ^{14}C age ranges were used to calibrate the magnetostratigraphic data. Finally, the magnetic field intensity, declination, and inclination were used for the age tuning by comparing available magnetostratigraphic records and models (Mix et al., 2003; Pavón-Carrasco et al., 2014; Liu et al., 2020).

4. Results and interpretations

The stratigraphy of the studied profile is divided into two intervals: The upper fine-grained deposits extend from 0 to 184 cm depth, followed by coarse-grained deposits down to the base of the profile at a depth of 420 cm (Table S1, S2; Figs. 2, 3, S4).

4.1. Clay Pan (CP)

4.1.1. CP geochemistry and sedimentology

The Herradura clay pan experienced recent flooding in June 2017 (Fig. S5). Subsequent evaporation has resulted in the formation of mud chips and desiccation polygons (Fig. S6). Eight months after the flooding event, exposed curled-up mud chips have been intensely eroded at their edges (Fig. S1E). A distinct base of the recent depositional layer is not visible, as the grain size distribution of the surface layer is analogous to the stratigraphy of the upper 184 cm. This interval is characterized by laminated layers dominated by clayey silt and interbedded sand, and each layer exhibits unimodally grain size distributed (Table S1; Fig. 3B, S4). The similarity between the upper interval stratigraphy and the recent deposition suggests that the upper interval also consists of clay pan deposits (CP), where episodic overland flow deposits are associated with rain events of varying intensity. The CP stratigraphy can be divided into a lower CP interval (104–184 cm depth) with few sand-rich between thick silt-rich layers and an upper CP interval containing desiccation cracks at the surface, sand-filled streamlets at ~45 cm depth, and overall more abundant sand-rich layers. The siliciclastic mineralogy of the CP deposits determined through semi-quantitative XRD is dominated by quartz, feldspars, and phyllosilicates including smectite, illite, chlorite, and sepiolite; showing no systematic change in content with depth (Fig. 2C; S7).

The μ-XRF element abundances and ratios are here used as environmental proxies (e.g., Diederich et al., 2020; Liu et al., 2023). The Zr/Rb ratio and the magnetic susceptibility (κ_{LF}) correlate with the grain size derived from sieving (Fig. 3). The Rb/Sr ratio is used in lake sediments as a proxy for weathering within the catchment area, since Rb is less readily released from bedrock by chemical weathering than Sr (Liu et al., 2023). Generally, the Rb/Sr in the CP interval follows the grain size proxies (κ_{LF} and Zr/Rb) but between 110 and 140 cm depth it shows significantly lower values (Fig. 3C, D). The XRD results reveal that gypsum ($CaSO_4 \cdot 2H_2O$) is the dominant mineral of the water-soluble fraction, referred to as solubles ranging between 8 and 18 wt%. Ca and S abundances from μ-XRF show a moderate positive correlation of $R^2 = 0.66$, indicating that Ca is not only present in gypsum but might be present in other minerals such as plagioclase, phyllosilicates, and carbonates (Fig. 2C, 3E).

Salinity by EC measurements together with Na^+, Cl^-, and NO_3^- concentration by IC analysis are elevated between 40 and 150 cm depth,
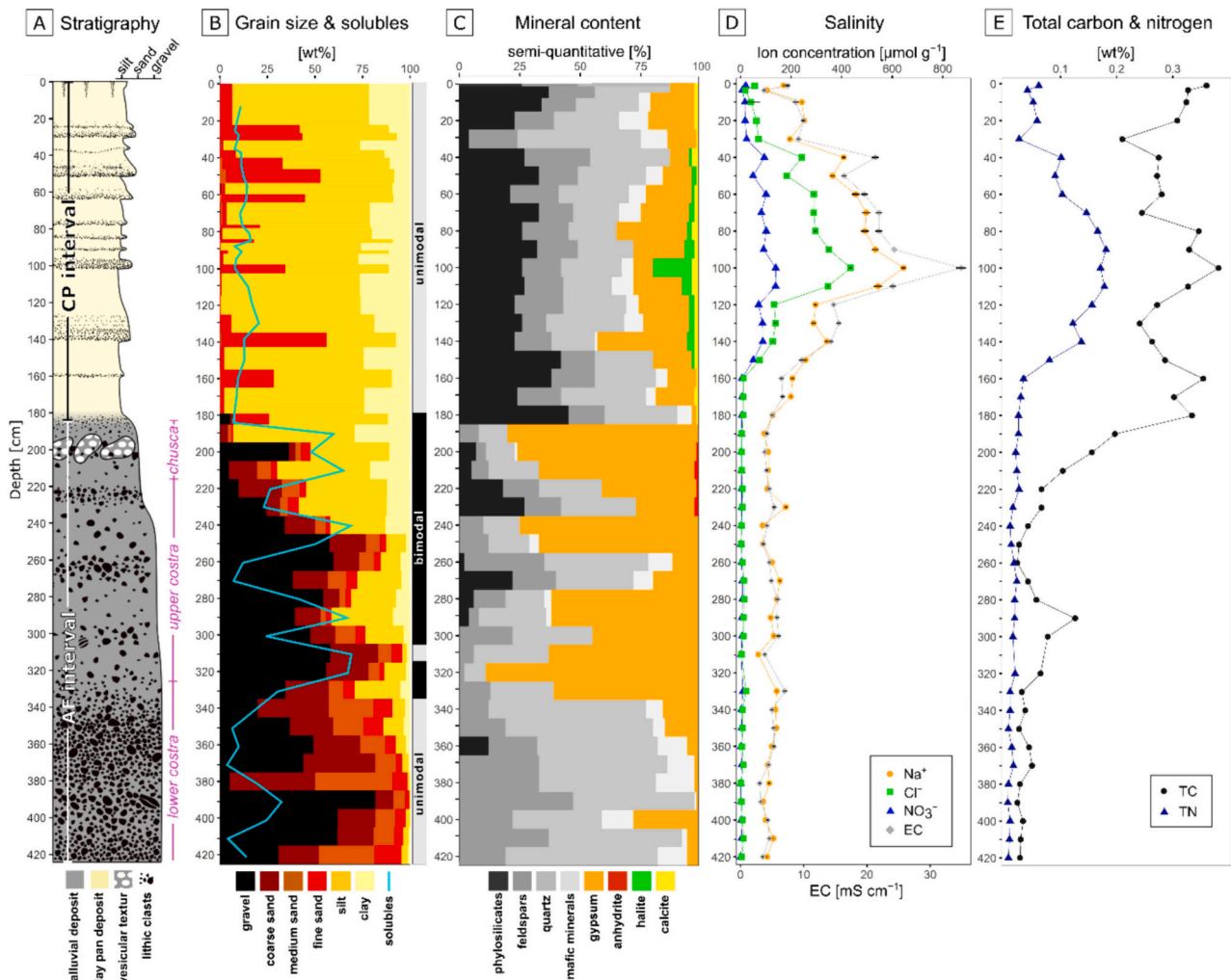
Fig. 2. Sedimentological and geochemical results covering the full profile. A) Stratigraphic column, including sedimentological features based on field observations. The lithic clasts density in the AF interval indicates the observed degree of clast support i.e., soluble content. B) Grain size distribution of the lithic fraction and soluble content of the total sample. Uni- and bimodal grain size distribution is shown in black and gray columns. C) Semi-quantitative mineral content. D) Na$^+$, Cl$^-$, NO$_3^-$ ion concentration and electrical conductivity (EC). E) Total carbon (TC) and total nitrogen (TN) concentration.

reaching a maximum at ~100 cm, where halite (NaCl) was detected by XRD. The distribution of the nitrate, presumably nitratine (NaNO$_3$), is mirrored by the total nitrogen content (TN). The $\delta^{15}N_{TN}$ values, being close to the atmospheric value of 0 ‰, similar to most of the nitrate deposits within the soils of the Atacama Desert, originate dominantly from photochemical reactions in the atmosphere (Fig. S8) (Böhlke et al., 1997; Michalski et al., 2004). In the CP interval, the salinity peak around 100 cm depth is presumably not caused by rainwater infiltration down to this depth as it is interpreted for typical soils based on Ma-old alluvial deposits in the Atacama Desert, as the clay pan sediment are less permeable and the clay pan setting is dominated by rapid evaporation (Ewing et al., 2006, 2008; Finstad et al., 2016). Rather, it could indicate a major shift in environmental conditions, which is also seen in the change in sedimentology.

The TC is dominated by carbonates (calcite) detected with XRD (Fig. 2). Due to the lack of bedrock- or plant-derived soil carbonate in the catchment area (Amundson et al., 2012; Domagala et al., 2016), we interpret the elevated carbonate content in the CP deposits to result from atmospheric CO$_2$ uptake during flooding events followed by in-situ carbonate precipitation during evaporation (Quade et al., 2007). The $\delta^{13}C_{bulk}$ value is a mix of carbonate and organic carbon and reflects the overall carbonate dominance as the values are on average positive (1.15 ‰) and close to the $\delta^{13}C_{carbonate}$ values (Fig. S8). The mean $\delta^{13}C_{carbonate}$

value of 3.5 ‰ reflects the formation of carbonate at isotopic equilibrium with atmospheric CO$_2$ (Quade et al., 2007), suggesting that the carbonate is primarily of abiotic origin. The mean $\delta^{18}O_{carbonate}$ value of −1.5 ‰ is close to the values of rainwater (−1.2 to −4.4 ‰) near 1000 m a.s.l. or fog (−1.9 ‰) (Aravena et al., 1989; Jordan et al., 2019) and typical for evaporitic environments (Quade et al., 2007).

4.1.2. CP chronology

No microfossils (e.g., diatoms) or phytoliths or anything else suitable for biostratigraphy was found in the profile. The only macroscopic biological remains found are plant seeds within the upper 104 cm depth, occurring at higher concentrations in the most fine-grained horizons with the highest abundance at 3.5 cm and 40 cm depth (Fig. 3F). All seeds are from the C3-plant *Huidobria fruticosa*, based on the comparison with modern seeds found at the western slopes of Cerro de las Tetas, 15 km southwest of the Herradura clay pan, but none have been reported in its current catchment area (Fig. 1, S9) (Placzek et al., 2014). Within the fine sand fraction we have also found glass shards, indicative for crypto tephra, along the entire CP interval, however, these were not suitable for further age dating.

The depositional ages of the upper CP deposits (<104 cm depth) were determined through radiocarbon age dating of *H. fruticosa* seeds (Table 1; Fig. S9), which are maximum ages, as the transport duration is
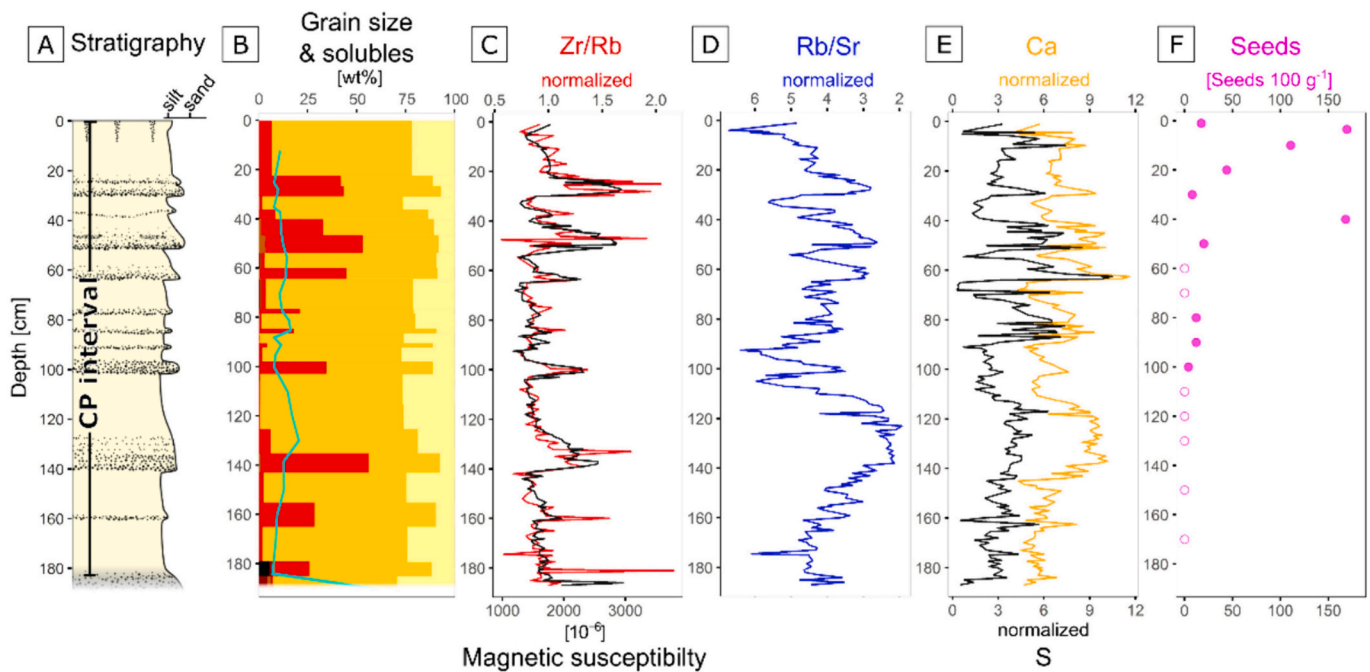
Fig. 3. Additional results covering the CP interval. A) Stratigraphy, for legend see Fig. 2. B) Grain size distribution and soluble content for the CP interval, for legend see Fig. 2. C) Zr/Rb ratio (red line) and magnetic susceptibility (κ_{LF}) given in SI units (10^{-6}) (black line) (see Fig. 4). D) Rb/Sr ratio. E) Ca and S concentrations. F) Huidobria fruticosa seed abundance (purple dots), purple circles indicate that no seeds were found. (For interpretation of the references to colour in this figure legend, the reader is referred to the web version of this article.)

Table 1
Radiocarbon dating results. Bold values were used for calibration of the magnetostratigraphic data.

Sample label	Depth [cm]	ETH lab code	C [µg]	$F^{14}C$	^{14}C age (BP) [a]	Age [cal BP] (68 %) [a]	Prob. [%]
						670–800	88
AC18-PP-2-5	3.5	111,657	40	0.896 ± 0.009	880 ± 90	870–900	12
						2470–2480	3
AC19-PP-25	25	108,627	21	0.724 ± 0.010	2600 ± 110	**2490–2760**	97
						2790–2820	13
AC19-PP-35	35	108,628	29	0.701 ± 0.008	2850 ± 90	**2850–3010**	87
						2770–2880	87
AC18-PP-40	40	111,658	100	0.707 ± 0.005	2790 ± 60	2900–2920	13
						4580–4600	2
						4620–5060	70
						5110–5130	4
AC-18-PP-80	80	111,659	20	0.582 ± 0.014	4340 ± 190	5180–5280	15
						9550–12,190	95
AC18-PP-90	90	111,660	12	0.304 ± 0.042	9560 ± 1100	12,220–12,460	5
AC19-PP-95	95	108,629	16	0.351 ± 0.012	8410 ± 270	**8990–9670**	100

unknown.

These ages were used to calibrate the magnetostratigraphic chronology. The results of paleomagnetic analyses show that the samples are very suitable for recording the paleomagnetic signal (Fig. S2, S3). The NRM intensity, which is fairly high, ranges from ~70 to 700 mAm^{-1} (Fig. 4A). Obtained relative paleo intensity (rPI) estimates, slope (NRM/ARM) and NRM(30 mT)/κ_{LF} show a fairly good match (Fig. 4B). The directions, inclinations and declinations of the characteristic remanent magnetization (ChRM), together with the corresponding maximum angular deviation (MAD) values are shown in Fig. 4C-E. Samples shown in fig. S2 are marked by red diamonds in the MAD record (Fig. 4E). Relative grain size changes are quite moderate (Fig. 4F). Coarser (finer) particles are linked to higher (lower) ratio of the ARM against the saturated remanent magnetization (SIRM), the latter represented by the low field magnetic susceptibility (κ_{LF}) (Fig. 4F, H). The content of hematite is fairly constant, represented by S-ratios around 0.92 (Fig. 4G), which is also indicated by the saturated and hard remanent magnetization (Fig. S3). No reversed inclinations are observed nor geomagnetic

events like the Mono Lake or the Laschamp could be identified. The age model was tuned by comparing available magnetostratigraphic records and models yielding the depositional ages of the entire CP deposits with its onset 19 ka ago (Mix et al., 2003; Pavón-Carrasco et al., 2014; Liu et al., 2020) (Figs. 5, 6). The resulting sedimentation rate from 90 to 184 cm depth is ~10 cm ka^{-1}, followed by a rapid decrease to ~2 cm ka^{-1} within 85–90 cm depth, which was either caused by reduced sedimentation or enhanced erosion (hiatus). At 0–85 cm depth a higher sedimentation rate of ~20 cm ka^{-1} was calculated.

The $^{10}Be/^9Be$ ratios show a low variation over the CP interval (Table 2; Fig. 7, S10A). Radioactive decay remains insignificant due to the young age of the CP compared to the ^{10}Be half-life. We derive an average ^{10}Be flux of $\Phi(^{10}Be_{dc}) = 1.2 \times 10^7$ atoms cm^{-2} a^{-1} and a calcium sulfate flux of $\Phi(CaSO_4) = 30$ g m^{-2} a^{-1} (Table 3).
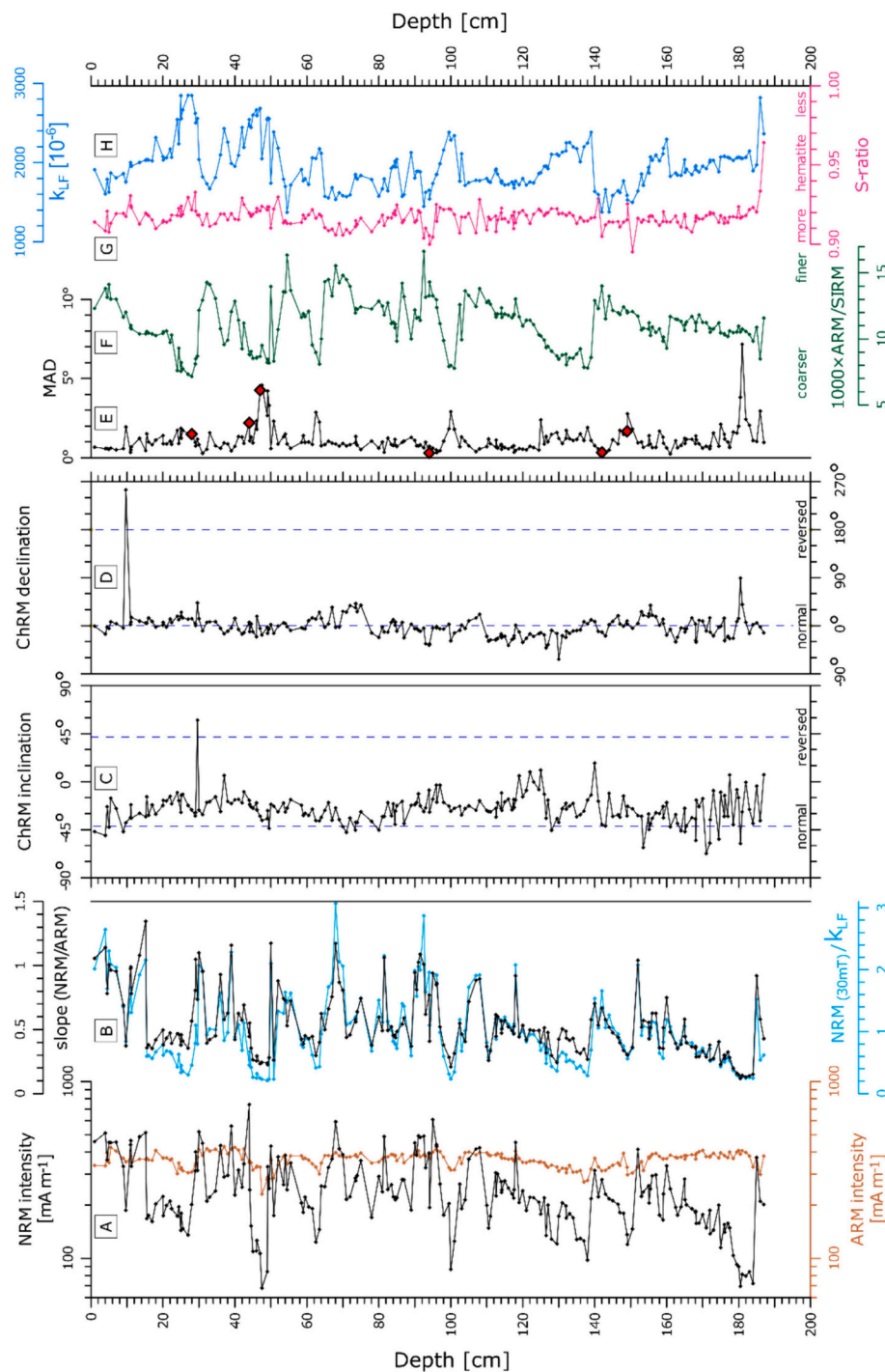
Fig. 4. Down-core plots of various paleo- and mineral magnetic parameters from Herradura sediments: A) NRM intensity (black) and ARM intensity (brown), the latter as a measure of the concentration of fine-grained magnetite, B) estimates of relative paleo intensity by the slope (NRM/ARM) of common alternating field demagnetization steps (black) and NRM after 30 mT normalized by low-field magnetic susceptibility (κ_{LF}) (blue), C) ChRM inclination, D) ChRM declination, E) precision of ChRM determination measured by the MAD, F) estimation of magnetic grain size (relative) using ARM over SIRM, G) S-ratio as a measure of relative hematite contribution, and H) overall concentration of magnetic minerals represented by low field magnetic susceptibility (κ_{LF}). NRM/ARM/ChRM: natural/ anhysteretic/characteristic remanent magnetization, MAD: maximum angular deviation, SIRM: saturated isothermal remanent magnetization. Red diamonds in E) mark samples with their detailed demagnetization results shown in fig. S2. Dashed vertical blue lines in C) and D) indicate inclination and declination, respectively, of a pure geocentric axial dipole, calculated for the study site. (For interpretation of the references to colour in this figure legend, the reader is referred to the web version of this article.)

4.2. Alluvial Fan (AF)

4.2.1. AF geochemistry and sedimentology

The lower interval (184–420 cm) is composed of poorly sorted clay- to gravel-sized siliciclastic sediments (Fig. 2B, C, Table S1, S2) with clasts up to 5 cm in diameter. Thus, we interpret the parent material of the lower interval as a distal alluvial deposit. The siliciclastic clasts are heavily cemented by fairly soluble salts, mainly gypsum and minor anhydrite (Fig. 2C). The soluble content decreases with depth, being between 184 and 215 cm depth ~ 50 wt% where gypsum and anhydrite
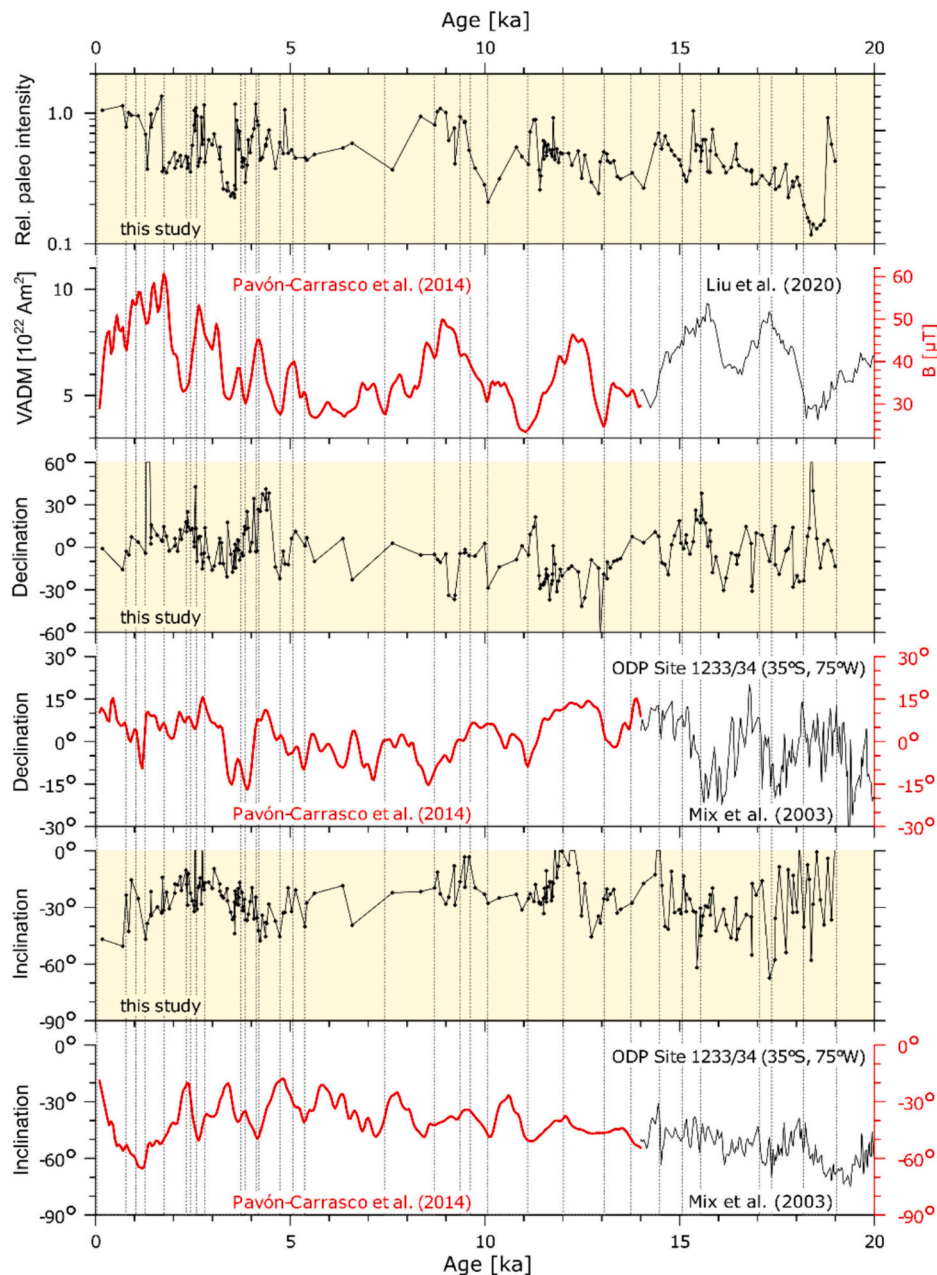
Fig. 5. Magnetostratigraphic results (light yellow background) including relative paleo intensity (slope (NRM/ARM)), declination (ChRM), and inclination (ChRM), along with the comparison with marine records (Mix et al., 2003; Liu et al., 2020) and geomagnetic field models (Pavón-Carrasco et al., 2014). VADM = Virtual axial dipole moment. Tie points are indicated by vertical dashed lines. (For interpretation of the references to colour in this figure legend, the reader is referred to the web version of this article.)

have formed a vesicular texture which is only visible fragmentarily (Fig. S1F). In 215–325 cm depth the soluble content averages 42 wt% (range 6–68 wt%) and below it decreases to 16 wt% in average (range 4–29 wt %) (Table S1; Fig. 2B). These features resemble the locally common inactive alluvial fan deposits (AF), accumulating dust and cemented by salts during prolonged hyperaridity (e.g., Ericksen, 1981; Ewing et al., 2006). The fragmented vesicular texture, being presumably part of the near surface *chusca* soil layer, could indicate that the former surface of the soil has been partially degraded during the initial clay pan flooding events and subsequent compaction. Below the deposits resembles a *costra* soil layer, which can be divided into an upper *costra* (215–325 cm) layer being more intense cemented by gypsum as the lower *costra* soil layer (325–420 cm). Its transition is also displayed in the grain size distribution shifts from a unimodal lower *costra* to bimodal in the upper

costra and *chusca* soil layer, with an additional local maximum in the silt fraction, and a higher standard deviation of the grain size distribution indicating a poorly sorting (Table S2; Fig. S6). Due to these features, we here define the *chusca* and upper *costra* soil layer as the upper AF interval and the lower *costra* soil layer as lower AF interval.

No significant amounts of highly soluble salts (e.g., chlorides or nitrates) were detected that would indicate a *caliche* horizon, typical for these deposits (Ericksen, 1981), and has been found in the Yungay valley in depth of around 1–2 m, which would be an equivalent depth in our profile of 3–4 m depth (Ewing et al., 2006; Arens et al., 2021). Either the *caliche* horizon has initially formed below 420 cm depth, or the highly soluble salts have been leached during the initial floodings of the basin. Total carbon (TC) and total nitrogen (TN) content decrease in the AF interval to values near or even below the detection limit (0.0124 wt%)
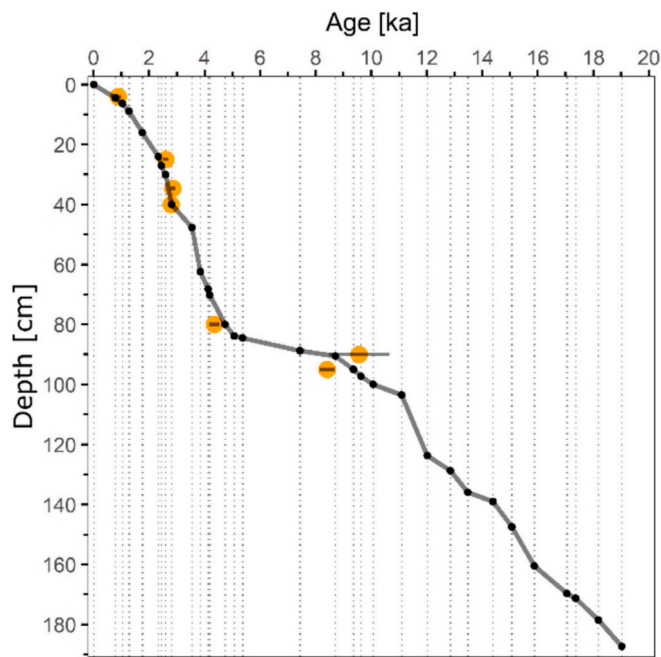
Fig. 6. CP depositional dating results. A) Depositional ages from radiocarbon dating of H. fruticose seeds (yellow dots with gray uncertainty bars) and magnetostratigraphy (gray line) with tie points (black dots and dashed vertical line) (Fig. 5). (For interpretation of the references to colour in this figure legend, the reader is referred to the web version of this article.)

and thus the isotope analysis reaches its limits, however a shift in $\delta^{18}O_{Carb}$ can be observed from the upper to the lower AF interval (325 cm depth).

4.2.2. AF chronology

While the ^{10}Be remains roughly constant in the CP deposits, it sharply decreases at the transition to the AF deposits (Fig. 7). We attribute this decrease to the exponential decay of ^{10}Be with depth. To correct for the grain size dependence of ^{10}Be, the ^{9}Be concentration is considered which correlates with the mean grain size of the fractions used for the Be extraction ($R^2 = 0.61$) (Fig. S10D-F). Consequently, the ^{10}Be/^{9}Be ratio is applied for depositional age dating. The law of radioactive decay, $N(t) = N_{t=19ka} \, e^{-\lambda d/S}$, is fitted to the data, where λ is the decay rate of ^{10}Be, $N(t)$ is the measured ^{10}Be/^{9}Be ratio within each soil layer and d the depth of each horizon (Fig. 8A). We assume the former AF surface at 184 cm depth to correspond with the beginning of the CP deposition 19 ka ago. Thus, the former AF surface ^{10}Be/^{9}Be ratio $N_{t=19\ ka}$ derived from the best fit yields $(0.78 \pm 0.16) \times 10^{-8}$. The corresponding average sedimentation rate $S = 63 \pm 13$ cm Ma^{-1} is used for deriving the depositional ages t = d/S for each layer. This results in the lowest AF horizon covered in the profile at 420 cm depth having an age of 3.8 ± 0.8 Ma (Fig. 8B). Since no ash layer nor glass shards were found in the AF interval for additional Ar/Ar or K/Ar dating, we consider dating using the ^{10}Be/^{9}Be ratio to be the most robust approach compared to e.g., only using the ^{10}Be concentrations. However, for comparison, we also present alternative dating approaches and their results in the supplemental materials. Two alternative age models are illustrated for comparison, using 1) the ^{10}Be concentrations alone, and 2) analogously to Wang et al. (2015), the ^{10}Be concentration corrected for the water-soluble fraction (Fig. S11), both yielding significantly higher ages than the ^{10}Be/^{9}Be approach.

5. Discussion

The Atacama Desert provides an extraordinary opportunity to study the dynamics of extreme arid landscapes persisting over geological

Table 2
Analytical results of meteoric ^{10}Be data of the entire profile.

Sample	Depth [cm]	Age [ka](CP) [Ma] (AF)	^{10}Be/^{9}Be [10^{-8} atoms atoms^{-1}]	^{10}Be [10^8 atoms g^{-1}]	^{9}Be [10^{16} atoms g^{-1}]
CP interval					
AC18-PP-0-2	1	0.17 ± 0.2	2.39 ± 0.09	5.64 ± 0.20	2.236 ± 0.098
AC18-PP-2-5	3.5	0.61 ± 0.2	2.47 ± 0.06	5.81 ± 0.14	2.359 ± 0.013
AC18-PP-10	10	1.35 ± 0.2	2.74 ± 0.08	5.48 ± 0.12	1.998 ± 0.032
AC18-PP-20	20	2.03 ± 0.2	2.62 ± 0.06	4.96 ± 0.11	1.895 ± 0.006
AC18-PP-30	30	2.58 ± 0.2	2.60 ± 0.06	3.75 ± 0.09	1.442 ± 0.01
AC18-PP-40	40	2.81 ± 0.2	2.75 ± 0.08	6.64 ± 0.18	2.417 ± 0.012
AC18-PP-50	50	3.58 ± 0.2	2.92 ± 0.07	5.64 ± 0.14	1.935 ± 0.007
AC18-PP-60	60	3.79 ± 0.2	3.04 ± 0.11	5.87 ± 0.13	1.933 ± 0.055
AC18-PP-70	70	4.18 ± 0.2	2.94 ± 0.08	6.53 ± 0.17	2.222 ± 0.025
AC18-PP-80	80	4.73 ± 0.2	3.06 ± 0.08	6.71 ± 0.15	2.196 ± 0.026
AC18-PP-90	90	8.35 ± 0.2	2.81 ± 0.07	6.14 ± 0.14	2.19 ± 0.011
AC18-PP-100	100	10.08 ± 0.2	2.57 ± 0.07	5.90 ± 0.15	2.292 ± 0.008
AC18-PP-110	110	11.39 ± 0.5	2.98 ± 0.07	6.16 ± 0.13	2.066 ± 0.013
AC18-PP-120	120	11.84 ± 0.5	3.03 ± 0.07	5.22 ± 0.11	1.721 ± 0.01
AC18-PP-130	130	12.96 ± 0.5	2.86 ± 0.06	4.66 ± 0.10	1.63 ± 0.006
AC18-PP-140	140	14.46 ± 0.5	2.80 ± 0.04	6.13 ± 0.08	2.187 ± 0.013
AC18-PP-150	150	15.23 ± 0.5	2.89 ± 0.07	6.26 ± 0.16	2.168 ± 0.002
AC18-PP-160	160	15.84 ± 0.5	2.76 ± 0.04	5.41 ± 0.07	1.961 ± 0.006
AC18-PP-170	170	17.12 ± 0.5	2.72 ± 0.04	5.50 ± 0.08	2.019 ± 0.015
AC18-PP-180	180	18.33 ± 0.5	2.73 ± 0.04	5.06 ± 0.07	1.853 ± 0.007
AF interval					
AC18-PP-190	190	0.11 ± 0.02	1.835 ± 0.041	2.697 ± 0.05	1.469 ± 0.018
AC18-PP-200	200	0.27 ± 0.05	0.92 ± 0.035	1.064 ± 0.04	1.156 ± 0.006
AC18-PP-210	210	0.43 ± 0.09	0.524 ± 0.015	0.552 ± 0.013	1.053 ± 0.017
AC18-PP-220	220	0.59 ± 0.12	0.314 ± 0.009	0.414 ± 0.012	1.319 ± 0.001
AC18-PP-230	230	0.75 ± 0.15	0.438 ± 0.012	0.585 ± 0.015	1.337 ± 0.009
AC18-PP-240	240	0.9 ± 0.18	0.995 ± 0.022	0.971 ± 0.021	0.976 ± 0.007
AC18-PP-250	250	1.06 ± 0.22	0.415 ± 0.015	0.343 ± 0.012	0.828 ± 0.004
AC18-PP-260	260	1.22 ± 0.25	0.283 ± 0.009	0.371 ± 0.012	1.313 ± 0.009
AC18-PP-270	270	1.38 ± 0.28	0.244 ± 0.008	0.562 ± 0.018	2.301 ± 0.018
AC18-PP-280	280	1.54 ± 0.31	0.348 ± 0.008	0.836 ± 0.018	2.401 ± 0.018
AC18-PP-290	290	1.7 ± 0.35	0.736 ± 0.016	0.881 ± 0.019	1.197 ± 0.006
AC18-PP-300	300	1.85 ± 0.38	0.484 ± 0.013	0.604 ± 0.016	1.248 ± 0.008
AC18-PP-310	310	2.01 ± 0.41	0.271 ± 0.01	0.259 ± 0.01	0.957 ± 0.004
AC18-PP-320	320	2.17 ± 0.45	0.147 ± 0.008	0.106 ± 0.006	0.72 ± 0.002

(continued on next page)

Table 2 (*continued*)

Sample	Depth [cm]	Age [ka](CP) [Ma] (AF)	^{10}Be/^{9}Be [10^{-8} atoms atoms^{-1}]	^{10}Be [10^8 atoms g^{-1}]	^{9}Be [10^{16} atoms g^{-1}]
AC18-PP-330	330	2.33 ± 0.48	0.154 ± 0.006	0.217 ± 0.008	1.415 ± 0.004
AC18-PP-340	340	2.49 ± 0.51	0.151 ± 0.057	0.153 ± 0.058	1.012 ± 0.004
AC18-PP-350	350	2.65 ± 0.54	0.112 ± 0.005	0.129 ± 0.006	1.156 ± 0.008
AC18-PP-360	360	2.8 ± 0.58	0.138 ± 0.004	0.126 ± 0.003	0.914 ± 0.005
AC18-PP-370	370	2.96 ± 0.61	0.38 ± 0.013	0.259 ± 0.009	0.68 ± 0.003
AC18-PP-380	380	3.12 ± 0.64	0.073 ± 0.012	0.029 ± 0.005	0.393 ± 0.001
AC18-PP-390	390	3.28 ± 0.67	0.147 ± 0.014	0.056 ± 0.005	0.379 ± 0.002
AC18-PP-400	400	3.44 ± 0.71	0.156 ± 0.013	0.149 ± 0.013	0.957 ± 0.002
AC18-PP-410	410	3.6 ± 0.74	0.37 ± 0.018	0.313 ± 0.015	0.845 ± 0.001
AC18-PP-420	420	3.75 ± 0.77	0.174 ± 0.005	0.104 ± 0.003	0.594 ± 0.006

Table 3

Sedimentation rates, CaSO$_4$- and ^{10}Be-fluxes for the different intervals and reference data. All fluxes including ^{10}Be and calcium sulfate fluxes calculated analogous to the ^{10}Be fluxes are given in supplement tables S3 and S4.

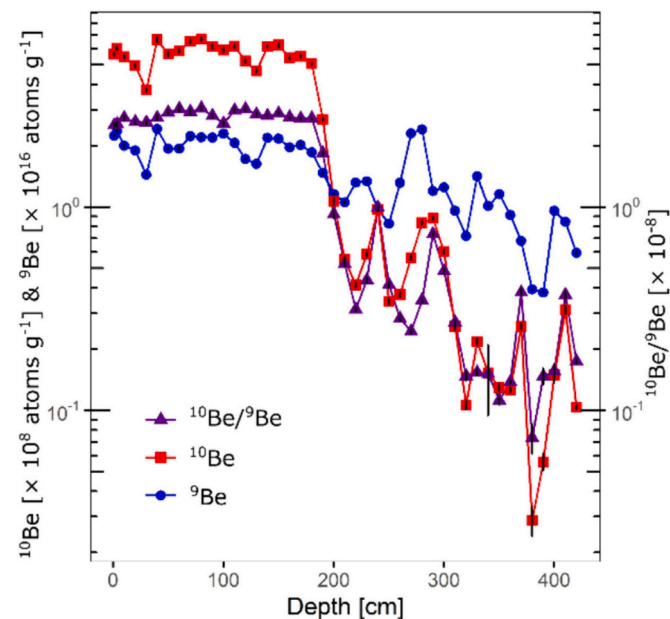|	Sedimentation-rate [m Ma^{-1}]	$\Phi(CaSO_4)$ [g m^{-2} a^{-1}]	$\Phi(^{10}Be_{dc})$ [atoms cm^{-2} a^{-1}]
Atacama Desert atmospheric deposition		0.5–1.5 (Ewing et al., 2006, Owen et al., 2013)	(3.7 ± 0.6) × 10^4 (Wang et al., 2015)
CP (0–184 cm)	100 (20–200)	30 (range 2–105)	1.2 × 10^7 (range 2.5 × 10^6–3.2 × 10^7)
AF (184–420 cm)	0.63	0.31 (range 0.04–0.65)	9.3 × 10^3 (range 1.3 × 10^3–2.7 × 10^4)

Fig. 7. Beryllium isotope concentrations and ratios (not corrected for radioactive decay) along the profile depth.

Average ^{10}Be fluxes are 3 orders of magnitudes lower than in the CP interval, with $\Phi(^{10}Be_{dc}) = 9.3 \times 10^3$ atoms cm^{-2} a^{-1}, while the average calcium sulfate flux is one order of magnitude lower, with $\Phi(CaSO_4) = 0.31$ g m^{-2} a^{-1} (Table 3).

timescales. Therefore, chronology is crucial. The AF interval of the Herradura record allows to reach back into the late Pliocene, while the CP interval covers the late Pleistocene and Holocene including the Marine Isotope Stage 1 (MIS 1, 0–14 ka) and part of the MIS 2 (14–19 ka) (Fig. 9). Due to the sedimentation rates of the AF interval ($\sim$1 m Ma^{-1}) versus the CP interval ($\sim$100 m Ma^{-1}) and their overall age difference, different dating methods for each are required to disentangle their respective climate histories. Furthermore, the deposition processes of both intervals are fundamentally different. The CP is dominated by a single process of episodic basin floodings during rare rain events. In contrast, the AF has formed by discontinuous alluvial deposition and by continuous accumulation of atmospheric dust and salts over millions of

years, resulting in a complex soil structure (Ewing et al., 2006; Arens et al., 2021) (Fig. 9). Within the entire Atacama Desert only three clay pans have been dated so far, only going back 10s and 100s ka (Ritter et al., 2019; Diederich et al., 2020; Wennrich et al., 2024). In contrast to the scattered clay pans, alluvial fans are almost ubiquitous in the Atacama Desert and reach ages of over several million years. However, dating alluvial deposits remains challenging and could strongly benefit from new approaches like the here applied meteoric ^{10}Be/^{9}Be method, which is discussed in the following.

5.1. Alluvial fan record

For the millions-year-old AF interval common dating methods e.g., ash deposits, biostratigraphy, or magnetostratigraphy are not applicable due to the absence of ash (including crypto tephra), fossils, or fine-grained fluviatile deposits (e.g., Ewing et al., 2006; Rech et al., 2006; Ritter et al., 2019). In-situ cosmogenic nuclide dating methods have been widely used to date surface ages and burial ages in the Atacama Desert (e.g., Ewing et al., 2006; Amundson et al., 2012; Jungers et al., 2013). Surface disturbance, erosion, and complex exposure history can significantly influence the dating outcome of depositional ages which warrants caution and requires good knowledge of the depositional environment (Jungers et al., 2013). As an alternative approach to dating these deposits, we here applied meteoric ^{10}Be/^{9}Be ratio-based method providing a continuous record of depositional ages. However, when ^{10}Be/^{9}Be ratio-based dating is applied to Atacama Desert sediments several aspects have to be considered.

First, it is essential to note that ^{9}Be is released from rocks through weathering, while ^{10}Be originates from the atmosphere (von Blanckenburg et al., 2012). Unlike in the CP interval, the decay-corrected ^{10}Be$_{dc}$ and ^{9}Be concentration of the AF deposits do not correlate well ($R^2 = 0.20$, Fig. S10B) and it cannot be excluded that this is due to variations in Be input in this environmental setting. Thus, the continuous sedimentation in this environmental context is only a first approximation of the AF chronostratigraphy. In fact, the alluvial fan deposition occurs episodically with hiatus in between, whereas the atmospheric input of salt and dust including ^{10}Be is added more continuously to the soil. Especially the former surface of the alluvial fan deposit where the stratigraphy transitions into the clay pan deposits, could signal such a hiatus, as cosmogenic nuclide dating has yielded surface sediments of alluvial fans in the Yungay valley with exposure ages of 0.3–1.1 Ma (Jungers et al., 2013; Placzek et al., 2014). The high ^{10}Be$_{dc}$ in the upper samples of the AF interval can also be indicative of a mixture with the clay pan deposits, being fine grained and concentrated with ^{10}Be during the initial clay pan flooding (Fig. 9, Table S4).

A size-depended particle migration after deposition due to rain events is possible, for which the ^{10}Be related to nm-sized atmospheric dust is more mobile than the ^{9}Be mainly related to μm-sized silicates.
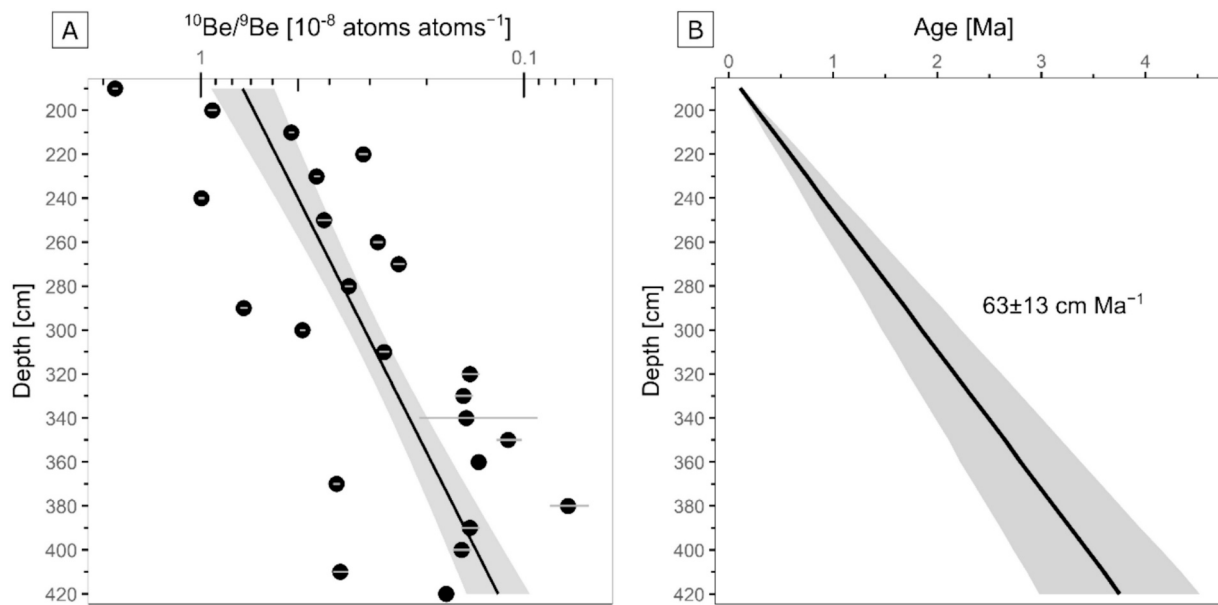
Fig. 8. AF depositional dating results. A) $^{10}Be/^{9}Be$ ratio (black dots) and their regression line (black line) as a function of depth for the AF interval. The band of uncertainty (gray) is calculated with a confidence interval of one standard deviation (1 SD). B) Depositional age as function of depth for the AF interval. The correlation including the 1 SD band of uncertainty is derived from the sedimentation rate.

Furthermore, it is conceivable that seismic shaking results in an analogous downward migration (Sager et al., 2020). This differential migration could explain the observed large variability in the $^{10}Be/^{9}Be$ ratio and the resulting dating. Hence, the chronostratigraphic interpretation of these hyperarid settings remains challenging due to potential post-depositional migration of soil constituents.

Thus far, only a single study, 150 km further north of the Herradura clay pan, determined a chronostratigraphy using single meteoric ^{10}Be concentration. This hyperarid location, analogous to our AF interval, yielded a maximum age of 6.6 ± 0.4 Ma at 225 cm depth (Wang et al., 2015). Applying the Wang et al. (2015) dating method, which is not corrected for ^{9}Be concentration, to our data yields a maximum age of 6.8 ± 1.1 Ma at an analogous depth compared to 3.8 ± 0.8 Ma with $^{10}Be/^{9}Be$ (Fig. S11). We attribute this large difference in maximum age to grain size variations affecting the single ^{10}Be concentrations, but not the ^{10}Be and ^{9}Be concentrations (Wittmann et al., 2012). Given the correlation between ^{10}Be and ^{9}Be in the CP interval and the correlation between ^{9}Be and the grain size, we recommend to use $^{10}Be/^{9}Be$ dating for the following paleoenvironmental reconstruction of the AF interval.

Based on the $^{10}Be/^{9}Be$ dating the average accumulation rates of $CaSO_4$ and ^{10}Be in the AF interval ($\Phi(CaSO_4) = 0.31$ g m^{-2} a^{-1}; $\Phi(^{10}Be_{dc}) = 9.3 \times 10^3$ atom cm^{-2} a^{-1}) are in the lower end of the atmospheric deposition rates calculated for the Atacama Desert, which, for ^{10}Be, are already one magnitude lower than the global average (5.7×10^5 atom cm^{-2} a^{-1}) (Ewing et al., 2006; Field et al., 2006; Wang et al., 2015) (Table 2). This can either point to particularly arid conditions in the Yungay valley or to partially removal by erosion.

The transition of lower to upper AF deposits between 320 and 330 cm depth, marked by an increase in soluble content, occurred 2.3 ± 0.5 Ma ago. This could be a result of a reduced salt leaching or an increasing salt input in the upper AF interval. A higher input could be caused by a more frequent fog occurrence, being a major salt source in the Atacama, introducing salts from the ocean into the desert (Voigt et al., 2020). The current situation with an upper fog boundary in this region ~1200 m a.s.l. allows fog to penetrate the Yungay valley, however, the stable isotope signature of the sulfates within the adjacent soils indicate only a minor influence of the fog as a salt supplier (Arens et al., 2021). Synchronously a drainage division occurred in the Yungay valley during the late Pliocene which was caused by local alluvial activity, that could have influenced the salt input into the Yungay valley (Amundson et al., 2012). The AF interval is likely part of these local alluvial infills and could be affected by this division, becoming hydrologically disconnected from the Andes. The higher $CaSO_4$ content in the upper interval is presumably related to a lower moisture availability during its formation i.e., a climatic change towards more arid conditions. This has been shown for soils along an aridity gradient within the Atacama Desert, where sulfate content correlates with aridity (Ewing et al., 2006). The shift from a clast- to a matrix-supported texture (Fig. 9), as well as the grain size distribution shifting from unimodal to bimodal could point also to an overall more arid condition (Fig. S4): The unimodal distribution in the lower AF interval points to a single transport mechanism dominated by alluvial transport, while the bimodal grain size distribution in the upper AF interval could point to a secondary input, most likely atmospheric dust (Vandenberghe, 2013). We assume that initially the alluvial material was clast-supported and underwent volumetric expansion through gypsum and minor lithic dust uptake. In addition, the upper AF interval contains remnants of a *chusca* horizon, which is a pedogenic feature typically for the hyperarid Atacama Desert and a good proxy for persistent and prolonged hyperarid conditions (Pfeiffer et al., 2021). This soil structure also indicates a very slow, or non-deposition of alluvial material (lithic clasts), and in this sense presents a hiatus. This potential transition to a drier climate at 2.3 ± 0.5 Ma is consistent with other paleo record data available for the Atacama Desert based on radiometric dating (including cosmogenic nuclides) situating this climate shift between 2 and 3 Ma ago (Hartley and Chong, 2002; Ewing et al., 2006; Amundson et al., 2012; Jordan et al., 2014; Wang et al., 2015; Ritter et al., 2018b). The climatic change is linked to an interplay between global cooling during the Pliocene resulting in a northern hemisphere glaciation ~2.75 Ma ago and long-term variability in the El Niño Southern Oscillation (ENSO), which stabilized ~2 Ma ago to present day condition (Ravelo et al., 2004; Amundson et al., 2012). For later wet phases which have been identified in paleo records further north we find no indication (Jordan et al., 2014; Wang et al., 2015), highlighting the complexity of the climate within the Atacama Desert. Another reason could be the poorly constrained chronology in the AF interval and its broad resolution.

Future investigation should apply additional dating methods like $^{26}Al/^{10}Be$ exposure dating and $^{10}Be/^{21}Ne$ burial dating to achieve a
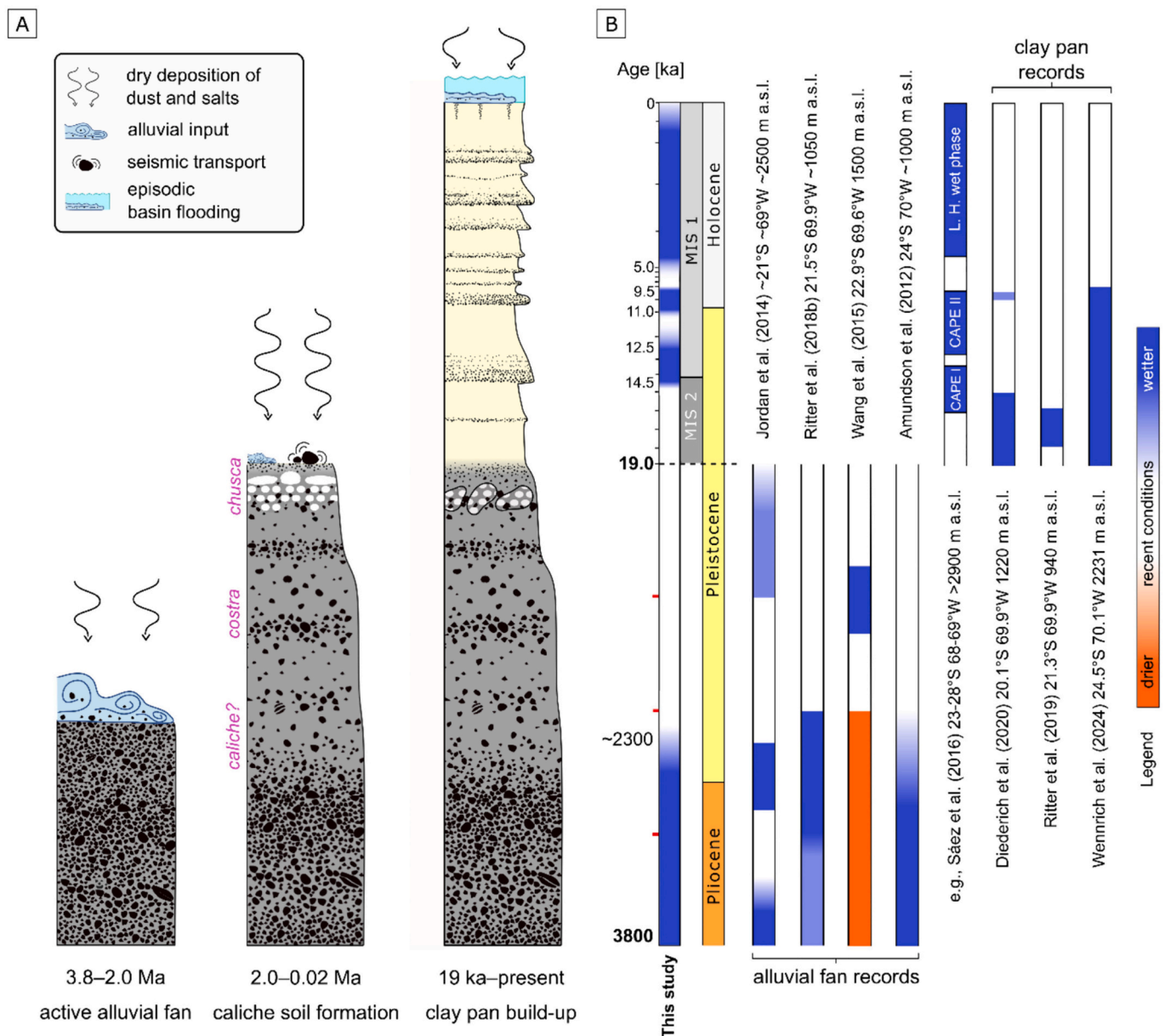
Fig. 9. A) Sketch of the Herradura stratigraphic buildup. 3.8–2.0: Ma arid conditions, active alluvial fan; 2.0–0.02 Ma: hyperarid conditions, reduced alluvial activity, accumulation of atmospheric dust, Atacama typical soil structure (caliche); 19 ka–present: basin formation and clay pan deposition by episodically flooding after rare rain events. Legend as in Fig. 2. B) Chronological columns with the Herradura record next to relevant paleo records including identified dry and wet phases like the Late Holocene (L. H.) wet phase and Central Andean Pluvial Events (CAPE I and CAPE II), Marine Isotope Stages (MIS), and the corresponding geological time episodes (ages in ka, black ticks in the CP interval represent 1 ka time interval, red ticks in the AF interval represents 1000 ka time interval). (For interpretation of the references to colour in this figure legend, the reader is referred to the web version of this article.)

more precisely constrained chronology of alluvial fan deposits. A combined dating approach could also give information about potential hiatus within the deposition history and post depositional soil processes. The exposure dating should be able to identify whether there is a significant hiatus and its duration at the border of the AF and CP intervals. Further efforts should be made to find adjacent ash layers which can be linked to the stratigraphy in the field or crypto tephra within the stratigraphy itself, to apply K/Ar or Ar/Ar dating for tuning the cosmogenic nuclide dating methods.

5.2. Clay pan record

The onset of the clay pan is related to the formation of an endorheic basin, preventing further drainage into the lower-lying Aguas Blancas

salar. We assume that the basin was subsequently flooded. However, the initial CP deposits recorded in our profile do not necessarily coincide with the base of the entire clay pan. Hence, the clay pan together with the basin could have formed earlier. Reasons for the formation could be outflow blocking through tectonic events, as known for other clay pans in the hyperarid Atacama Desert (Ritter et al., 2019; Diederich et al., 2020) and with a potential fault lying only ~1 km east of the clay pan (Domagala et al., 2016) (Fig. 1C). Alternatively, also alluvial activity can cause drainage division, which has been described for the Yungay valley before (Amundson et al., 2012).

For the CP deposits, which are too young for the meteoric ^{10}Be dating method, we observed a good correlation between the ^{10}Be and ^{9}Be concentration ($R^2 = 0.78$) yielding a relatively constant ratio throughout its deposition (Fig. S10A). This has also been shown for

various lacustrine and marine deposits over the past 8 Ma (Lebatard et al., 2010), and 12 Ma, respectively (Willenbring and von Blancken-burg, 2010). The fluxes for calcium sulfate are a hundred times higher ($\Phi(CaSO_4) = 30$ g m^{-2} a^{-1}) and for ^{10}Be a thousand times higher ($\Phi(^{10}Be_{dc}) = 1.2 \times 10^7$ atom cm^{-2} a^{-1}) in the CP interval compared to the AF interval, which can be explained by the different depositional environments, depositing more or less efficient fine-grained material which is associated to the Beryllium and the calcium sulfate. In a clay pan environment the dominating input of fine-grained sediment are flash floods or overland flows from the entire catchment area. In contrast, the alluvial fan is a less efficient depositional environment for fine-grained material, which is dominantly transported further down-stream. Remarkably, the CP depositional ^{10}Be flux also exceeds the fluxes derived from other materials collected around the globe, such as soil profiles, riverine solids, and marine records, by an order of magni-tude (e.g., Wang et al., 1996; Deng et al., 2021). Therefore, a detailed reconstruction of the paleoclimate aids in a better understanding of this unique environment.

The Yungay valley has undergone multiple climatic changes within the last 19 ka that can be deciphered from the CP record. We base our paleo reconstruction of the CP interval on different proxies including the grain size distribution, which is being used as a proxy for precipitation within the catchment area of a clay pan (e.g. Ritter et al., 2019; Die-derich et al., 2020; Wennrich et al., 2024). Silt-dominated fine-grained layers represent phases with minor flooding events and sand-dominated coarse-grained layers represent phases with moderate floodings caused by heavy rain events developing higher transport energies. These shifts in moisture availability are supported by the following additional proxies: 1) The shift in sedimentation rates in the Holocene, dropping after the Pleistocene down to ~2 cm ka^{-1} and increasing over the last 5 ka supports the dry phase in the early Holocene and more intense and/or more frequent flash floods during the late Holocene (Fig. 6A). 2) The elemental ratio Rb/Sr (Fig. 3C), indicative for weathering (e.g., Liu et al., 2023), reflect the pattern of the grain size distribution. Moreover, the Rb/Sr ratio reveals a sustained period of even lower Rb/Sr ratio 14.5–12.4 ka ago, supporting increased water availability during this period. 3) The increase of seed abundance during the late Holocene (Fig. 3E) coincides with other records in the coastal area, like the presence of rodent middens and alluvial fan activity (Vargas et al., 2006; Diaz et al., 2012). 4) The increase of NO$_3^-$ and Cl$^-$ begins with the transition from the Pleistocene to the Holocene, indicating a input from incised salt-containing alluvial fans by more abundant or more intense flash floods, capable of leaching these salts. Eroded alluvial fans are especially abundant in the southeastern catchment area (Fig. S5C). These channel incisions have been observed as a response in the study area after recent extraordinary rain events (Pfeiffer et al., 2021). Together, three wet phases can be identified in the CP interval (Fig. 9A, B). The two earlier wet phases (14.5–12.5 ka and 11.0–9.5 ka) and a ~ 5 ka long third phase during the late Holocene, while within the last centuries the aridity tends to increase again to present day conditions.

The variety of available paleo records around the hyperarid core of the Atacama Desert, including rodent middens, pollen, groundwater discharge deposits, and paleo shoreline reconstruction reveal a hetero-geneous precipitation pattern throughout the Atacama Desert during the late Pleistocene and Holocene (e.g., Grosjean et al., 2001; Sáez et al., 2016; de Porras et al., 2017; Pfeiffer et al., 2018; González-Pinilla et al., 2021). These records show that the intensity and frequency of wet conditions were primarily influenced by the proximity to the moisture sources. In the northern latitudes (16–20°S) in areas fed by water from the eastern mountains, the records suggest that the N-NE South Amer-ican Summer Monsoon significantly influences the regional rainfall patterns, with four wet phases: the Tauca phase (18–14 ka), the Coipasa phase (13–10 ka), early and late Holocene phases. Conversely, in the eastern mountains of the southern latitudes (23–28°S), the data in-dicates a SE summer monsoon, coupled with SW Pacific extratropical moisture influences brought by cutoff lows and moisture conveyor belts,

with only three wet phases: the Central Andean Pluvial Events (CAPE I: 15.9–13.8 ka; CAPE II: 12.7–9.7 ka) and a late Holocene wet phase. The late Pleistocene wet phases are attributed to a complex interaction be-tween North Atlantic sea surface temperature, anomalies in the Pacific sea surface temperature leading to La Niña-like states, and increased local summer insolation, all influencing the South American summer monsoon (González-Pinilla et al., 2021). For the Holocene, in the eastern Atacama Desert both in the north (González-Pinilla et al., 2021) and in the south (Sáez et al., 2016), the records imply that the orbital forcing became more dominant, influencing the ENSO, resulting in Eastern Pacific sea surface temperature fluctuation (Sáez et al., 2016; González-Pinilla et al., 2021).

In the western sectors of the hyperarid core of the Atacama Desert which do not receive runoff from the Andes mountains, the influence of the major moisture sources becomes less clear, as records are sparse. Here, clay pans have been proven suitable as valuable records of pre-cipitation proxies including sediment grain size, element ratios, and biomarkers including diatoms, phytoliths, and lipids (Ritter et al., 2019; Diederich et al., 2020; Wennrich et al., 2024). In the northern part, at 20°S, the Huara clay pan is influenced by the N-NE South American Summer Monsoon (tropical continental) and the SW Pacific extra-tropical (temperate maritime) moisture sources (Diederich et al., 2020). In the central Atacama Desert, at 21.5°S, the PAG clay pan reveals a precipitation pattern asynchronous to the South American Summer Monsoon but can be linked with the sea surface temperature offshore North Chile and Peru, connected to the ENSO (tropical maritime) (Ritter et al., 2019). Further south of the Yungay valley, in the Paranal clay pan (24.5°S, 2231 m a.s.l.), precipitation occurrence and intensity based on clay pan flooding analyzed via satellite imaging over the past 30 years (Wennrich et al., 2024). These flooding events can be correlates with recent ENSO variabilities indicating it as the main driver for heavy rain events in the catchment area. During the late Pleistocene and Holocene the chronostratigraphy of this clay pan deposit roughly links coarse-grained sediments, elevated diatom, phytolith, and lipid biomarker concentration within the deposits to enhanced moisture availability which could be related with the CAPEs (Wennrich et al., 2024).

The Herradura record lies in a key position to provide a link between southern and northern clay pan records helping to refine the spatial influences and temporal variability of the different weather systems affecting the Atacama Desert, such as the South American summer monsoon and the ENSO (Sáez et al., 2016; Houston and Latorre, 2022). This is particularly evident in the well constrained chronology of the upper 104 cm CP interval, combining radiocarbon dating with magne-tostratigraphy. Below, we have to solely rely on the magneto-stratigraphy, resulting in a reduced precision of the chronology. However, the commonality of the CP record with the adjacent records suggests a climatological connection between the Yungay valley, the southern Pre-Cordillera, and the southern Coastal Cordillera (e.g., Grosjean et al., 2001; Maldonado et al., 2005; Sáez et al., 2016; Wenn-rich et al., 2024). The two earlier wet phases identified in the CP record roughly coincide with the CAPEs (Quade et al., 2008), indicating a mutual moisture source during this period that affected the Yungay Valley. The temporal offset could be due to the distance from the moisture source of the CAPEs, which had only limited influence on this area. However, the less constrained chronology in the lower CP interval warrants further investigation to verify this. During the Holocene, the sedimentation rate increased from ~2 to 20 cm ka^{-1} at around 5 ka which aligns with records around the southern Atacama Desert and western slopes of the Andes which can be linked to ENSO regime shifts (Sáez et al., 2016; González-Pinilla et al., 2021).

The comparison of the CP record with other available clay pan re-cords within the Atacama Desert, the records further north (PAG ~280 km north, Huara ~445 km north) show significant differences in their precipitation history (Ritter et al., 2019; Diederich et al., 2020). Espe-cially within the late Holocene, the lack of sedimentation or a deflation resulting in a hiatus for the last 6 to 8 ka in both records indicating no or

very little flash floods, synchronous to the highest sedimentation rate within the CP underlines the heterogeneity (Ritter et al., 2019; Diederich et al., 2020). The most adjacent Paranal clay pan, ~50 km south of the Yungay valley shows similarities with the CP record despite of its poorly constrained chronology. Both records share the same sequence of wet and dry phases in the late Pleistocene and in the Holocene. Especially the diatom and phytolith record of the Paranal clay pan shows significant similarities with the seed record, indicating an abundance increase in the late Holocene and a drop towards the present day (Wennrich et al., 2024). However, the intensity of the rain events in the late Pleistocene wet phase seems to differ significantly, where the Herradura clay pan is dominated by sand/silt versus the Paranal deposit encompasses gravel, indicating alluvial debris flow into the clay pan during this period (Wennrich et al., 2024). This points to less extreme rain events affecting the Herradura clay pan compared to the Paranal clay pan during this period. Reasons for the different precipitation intensities could be the distance to the southern moisture sources (temperate maritime, i.e., cut-off lows and temperate continental, i.e., SE South American summer monsoon). In general, also the elevation difference of over 1000 m between both clay pans presumably plays an important role, as precipitation increases with increasing elevation exceeding 20 mm a^{-1} at 2300 m a.s.l. (Houston and Hartley, 2003). The comparison of clay pan records within the hyperarid core of the Atacama Desert supports the heterogeneous precipitation pattern in the region (Ritter et al., 2019; Diederich et al., 2020; Wennrich et al., 2024). Furthermore, the higher sedimentation rates of the southern clay pans point to the overall higher precipitation within their catchments, indicating a northward increase of aridity for the last 19 ka. Unfortunately, the northern and southern records do not overlap for long timespans, which warrants further investigations on clay pan records in the south, reaching further back in time to better comprehend the climate controls in the Atacama Desert within its past to allow predictions for future climate change.

6. Conclusion

The challenge of reconstructing the climatic history of the Atacama Desert over millions of years was addressed by a meteoric $^{10}Be/^{9}Be$ dating method, novel for soils, which formed under hyperaridity and capable of correcting for grain-size effects on the determined depositional ages. In contrast, the overlying CP deposits are dominated by relatively rapid deposition by flash floods, being too young for the $^{10}Be/^{9}Be$ dating method. However, these fine-grained sediments are suitable for magnetostratigraphy and with the occurrence of the *H. fruticosa* seeds it was possible to conduct radiocarbon dating. Caution is advised as the chronology is limited, as the lower CP interval relies solely on the magnetostratigraphy and lacks independent tie points. This is also true for the AF interval, where we only have the ^{10}Be dating. Nonetheless, both record types contribute to unraveling the evolution of the depositional environment. The alluvial fan deposits, in particular, integrate long-term climate signals spanning millions of years, while the clay pan deposits offer insights into episodic events on local and regional scales over millennial and orbital timescales. Together with different paleo environmental proxies, the combined record provides new dating tools and perspectives on the climate in the hydrologically discrete Coastal Cordillera responding to the temporally and spatially variable climate system of the Atacama Desert over the course of 3.8 Ma. Hence, our study is of great importance for studies investigating habitability under extreme aridity and biomarker preservation (e.g. Schulze-Makuch et al., 2018; Azua-Bustos et al., 2023), which require a profound understanding of soil processes and past environmental conditions as well as their regional variability in the Atacama Desert.

CRediT authorship contribution statement

Felix L. Arens: Writing – review & editing, Writing – original draft, Visualization, Validation, Resources, Project administration,

Methodology, Investigation, Formal analysis, Data curation, Conceptualization. **Jenny Feige:** Writing – review & editing, Writing – original draft, Methodology, Investigation, Funding acquisition, Formal analysis, Data curation. **Alessandro Airo:** Writing – review & editing, Writing – original draft, Supervision, Project administration, Investigation, Conceptualization. **Christof Sager:** Writing – review & editing, Methodology, Investigation, Formal analysis, Data curation. **Lutz Hecht:** Methodology, Data curation. **Lucas Horstmann:** Writing – review & editing, Methodology, Formal analysis. **Felix E.D. Kaufmann:** Methodology, Formal analysis. **Johannes Lachner:** Methodology, Formal analysis, Data curation. **Thomas Neumann:** Writing – review & editing, Validation, Resources. **Norbert Nowaczyk:** Writing – review & editing, Resources, Methodology, Formal analysis, Data curation. **Ferry Schiperski:** Writing – review & editing, Methodology, Data curation. **Peter Steier:** Methodology, Formal analysis, Data curation. **Alexandra Stoll:** Writing – review & editing, Methodology, Investigation. **Ulrich Struck:** Methodology, Formal analysis. **Bernardita Valenzuela:** Writing – review & editing, Resources. **Friedhelm von Blanckenburg:** Writing – review & editing, Data curation. **Hella Wittmann:** Writing – review & editing, Methodology, Data curation. **Lukas Wacker:** Writing – review & editing, Methodology, Formal analysis, Data curation. **Dirk Wagner:** Writing – review & editing, Resources. **Pedro Zamorano:** Writing – review & editing, Resources. **Dirk Schulze-Makuch:** Writing – review & editing, Supervision, Resources, Funding acquisition.

Appendix A. Supplementary data

Supplementary data to this article can be found online at https://doi.org/10.1016/j.gloplacha.2024.104576.

References

Akhmadaliev, S., Heller, R., Hanf, D., Rugel, G., Merchel, S., 2013. The new 6 MV AMS-facility DREAMS at Dresden. Nucl. Instrum. Methods Phys. Res., Sect. B 294, 5–10.

Amundson, R., Dietrich, W., Bellugi, D., Ewing, S., Nishiizumi, K., Chong, G., Owen, J., Finkel, R., Heimsath, A., Stewart, B., Caffee, M., 2012. Geomorphologic evidence for

the late Pliocene onset of hyperaridity in the Atacama Desert. Geol. Soc. Am. Bull. 124, 1048–1070.

Aravena, R., Suzuki, O., Pollastri, A., 1989. Coastal fog and its relation to groundwater in the IV region of northern Chile. Chemical Geology: Isotope Geoscience section 79, 83–91.

Arens, F.L., Airo, A., Feige, J., Sager, C., Wiechert, U., Schulze-Makuch, D., 2021. Geochemical proxies for water-soil interactions in the hyperarid Atacama Desert, Chile. CATENA 206, 105531.

Azua-Bustos, A., Fairén, A.G., González-Silva, C., Prieto-Ballesteros, O., Carrizo, D., Sánchez-Garcínez, M.Á., Escudero, C., Muñoz-Iglesias, V., others, 2023. Dark microbiome and extremely low organics in Atacama fossil delta unveil Mars life detection limits. Nat. Commun. 14, 808.

Bartz, M., Walk, J., Binnie, S.A., Brill, D., Stauch, G., Lehmkuhl, F., Hoffmeister, D., Brückner, H., 2020. Late Pleistocene alluvial fan evolution along the coastal Atacama Desert (N Chile). Glob. Planet. Chang. 190, 103091.

Blott, S.J., Pye, K., 2001. GRADISTAT: a grain size distribution and statistics package for the analysis of unconsolidated sediments. Earth Surf. Process. Landf. 26, 1237–1248.

Böhlke, J.K., Ericksen, G.E., Revesz, K., 1997. Stable isotope evidence for an atmospheric origin of desert nitrate deposits in northern Chile and southern California, USA. Chem. Geol. 136, 135–152.

Bourles, D., Raisbeck, G.M., Yiou, F., 1989. 10Be and 9Be in marine sediments and their potential for dating. Geochim. Cosmochim. Acta 53, 443–452.

Cereceda, P., Larrain, H., Osses, P., Farías, M., Egaña, I., 2008. The spatial and temporal variability of fog and its relation to fog oases in the Atacama Desert, Chile. Atmos. Res. 87, 312–323.

Chmeleff, J., von Blanckenburg, F., Kossert, K., Jakob, D., 2010. Determination of the 10Be half-life by multicollector ICP-MS and liquid scintillation counting. Nucl. Instrum. Methods Phys. Res., Sect. B 268, 192–199.

Clarke, J.D.A., 2006. Antiquity of aridity in the Chilean Atacama Desert. Geomorphology 73, 101–114.

Davila, A.F., Schulze-Makuch, D., 2016. The last possible Outposts for Life on Mars. Astrobiology 16, 159–168.

Davis, M., Matmon, A., Placzek, C.J., McIntosh, W., Rood, D.H., Quade, J., 2014. Cosmogenic nuclides in buried sediments from the hyperarid Atacama Desert, Chile. Quat. Geochronol. 19, 117–126.

de Porras, M.E., Maldonado, A., Pol-Holz, R. de, Latorre, C., Betancourt, J.L., 2017. Late Quaternary environmental dynamics in the Atacama Desert reconstructed from rodent midden pollen records. J. Quat. Sci. 32, 665–684.

Deng, K., Wittmann, H., Hsieh, M.-L., Yang, S., von Blanckenburg, F., 2021. Deposition and retention of meteoric 10Be in Holocene Taiwan river terraces. Quat. Sci. Rev. 265, 107048.

Diaz, F.P., Latorre, C., Maldonado, A., Quade, J., Betancourt, J.L., 2012. Rodent middens reveal episodic, long-distance plant colonizations across the hyperarid Atacama Desert over the last 34,000 years. J. Biogeogr. 39, 510–525.

Diederich, J.L., Wennrich, V., Bao, R., Büttner, C., Bolten, A., Brill, D., Buske, S., Campos, E., Fernández-Galego, E., Gödickmeier, P., Ninnemann, L., Reyers, M., Ritter, B., Ritterbach, L., Rolf, C., Scheidt, S., Dunai, T.J., Melles, M., 2020. A 68 ka precipitation record from the hyperarid core of the Atacama Desert in northern Chile. Glob. Planet. Chang. 184, 103054.

Domagala, J.P., Escribano, J., La Cruz, R. de, Saldias, J., Joquera, R., 2016. Cartas Blanco Encalada y Pampa Remiendos, Region de Antofagasta. Servicio Nacional de Geología Básica, 187–188.

Dunai, T.J., González, L., G., Juez-Larré, J, 2005. Oligocene–Miocene age of aridity in the Atacama Desert revealed by exposure dating of erosion-sensitive landforms. Geology 33, 321–324.

Ericksen, G.E., 1981. Geology and Origin of nitrate deposition in Atacama Desert. U.S. Geological Survey Professional Paper 37:1188.

Evenstar, L.A., Mather, A.E., Hartley, A.J., Stuart, F.M., Sparks, R.S.J., Cooper, F.J., 2017. Geomorphology on geologic timescales: Evolution of the late Cenozoic Pacific paleosurface in Northern Chile and Southern Peru. Earth Sci. Rev. 171, 1–27.

Ewing, S.A., Sutter, B., Owen, J., Nishiizumi, K., Sharp, W., Cliff, S.S., Perry, K., Dietrich, W., McKay, C.P., Amundson, R., 2006. A threshold in soil formation at Earth's arid–hyperarid transition. Geochim. Cosmochim. Acta 70, 5293–5322.

Ewing, S.A., Yang, W., DePaolo, D.J., Michalski, G., Kendall, C., Stewart, B.W., Thiemens, M., Amundson, R., 2008. Non-biological fractionation of stable ca isotopes in soils of the Atacama Desert, Chile. Geochim. Cosmochim. Acta 72, 1096–1110.

Field, C.V., Schmidt, G.A., Koch, D., Salyk, C., 2006. Modeling production and climate-related impacts on 10Be concentration in ice cores. J. Geophys. Res. Atmos. 111.

File, P.D., others, 2000. International Centre for Diffraction Data. Swarthmore, Pa, p. 19081.

Finstad, K., Pfeiffer, M., Amundson, R., 2014. Hyperarid Soils and the Soil Taxonomy. Soil Sci. Soc. Am. J. 78, 1845–1851.

Finstad, K., Pfeiffer, M., McNicol, G., Barnes, J., Demergasso, C., Chong, G., Amundson, R., 2016. Rates and geochemical processes of soil and salt crust formation in Salars of the Atacama Desert, Chile. Geoderma 284, 57–72.

Garreaud, R.D., Molina, A., Farias, M., 2010. Andean uplift, ocean cooling and Atacama hyperaridity: a climate modeling perspective. Earth Planet. Sci. Lett. 292, 39–50.

González-Pinilla, F.J., Latorre, C., Rojas, M., Houston, J., Rocuant, M.I., Maldonado, A., Santoro, C.M., Quade, J., Betancourt, J.L., 2021. High-and low-latitude forcings drive Atacama Desert rainfall variations over the past 16,000 years. Sci. Adv. 7, eabg1333.

Grosjean, M., van Leeuwen, J.F.N., van der Knaap, Willem, Oscar, Geyh, M.A., Ammann, B., Tanner, W., Messerli, B., La Núñez, Valero-Garcés, B.L., Veit, H, 2001. A 22,000 14C year BP sediment and pollen record of climate change from Laguna Miscanti (23 S), northern Chile. Glob. Planet. Chang. 28, 35–51.

Hartley, A.J., Chong, G., 2002. Late Pliocene age for the Atacama Desert: Implications for the desertification of western South America. Geol 30, 43.

Hogg, A.G., Heaton, T.J., Hua, Q., Palmer, J.G., Turney, C.S.M., Southon, J., Bayliss, A., Blackwell, P.G., Boswijk, G., Bronk Ramsey, C., et al., 2020. SHCal20 Southern Hemisphere Calibration 0–55 000 years cal BP. Radiocarbon 62, 759–778.

Houston, J., 2006a. Evaporation in the Atacama Desert: an empirical study of spatio-temporal variations and their causes. J. Hydrol. 330, 402–412.

Houston, J., 2006b. Variability of precipitation in the Atacama Desert: its causes and hydrological impact. Int. J. Climatol. 26, 2181–2198.

Houston, J., Hartley, A.J., 2003. The central Andean west-slope rainshadow and its potential contribution to the origin of hyper-aridity in the Atacama Desert. Int. J. Climatol. 23, 1453–1464.

Houston, J., Latorre, C., 2022. The role of the non-stationary Andean Dry Diagonal in paleoclimate reconstructions. Hydrol. Process. 36.

Jordan, T.E., Kirk-Lawlor, N.E., Blanco, N.P., Rech, J.A., Cosentino, N.J., 2014. Landscape modification in response to repeated onset of hyperarid paleoclimate states since 14 Ma, Atacama Desert, Chile. Bulletin 126, 1016–1046.

Jordan, T.E., Herrera, L., C., Godfrey, L.V., Colucci, S.J., Gamboa P., C., Urrutia M., J., González L., G., Paul, J.F, 2019. Isotopic characteristics and paleoclimate implications of the extreme precipitation event of March 2015 in northern Chile. andgeo 46, 1.

Jungers, M.C., Heimsath, A.M., Amundson, R., Balco, G., Shuster, D., Chong, G., 2013. Active erosion–deposition cycles in the hyperarid Atacama Desert of Northern Chile. Earth Planet. Sci. Lett. 371-372, 125–133.

Korschinek, G., Bergmaier, A., Faestermann, T., Gerstmann, U.C., Knie, K., Rugel, G., Wallner, A., Dillmann, I., Dollinger, G., von Gostomski, C.L., others, 2010. A new value for the half-life of 10Be by heavy-ion elastic recoil detection and liquid scintillation counting. Nucl. Instrum. Methods Phys. Res., Sect. B 268, 187–191.

Lal, D., Peters, B., 1967. Cosmic ray produced radioactivity on the Earth. Kosmische Strahlung II/Cosmic Rays II, 551–612.

Latorre, C., González, A.L., Quade, J., Fariña, J.M., Pinto, R., Marquet, P.A., 2011. Establishment and formation of fog-dependent Tillandsia landbeckii dunes in the Atacama Desert: evidence from radiocarbon and stable isotopes. J. Geophys. Res. 116.

Lebatard, A.-E., Bourlès, D.L., Braucher, R., Arnold, M., Duringer, P., Jolivet, M., Moussa, A., Deschamps, P., Roquin, C., Carcaillet, J., others, 2010. Application of the authigenic 10Be/9Be dating method to continental sediments: reconstruction of the Mio-Pleistocene sedimentary sequence in the early hominid fossiliferous areas of the northern Chad Basin. Earth Planet. Sci. Lett. 297, 57–70.

Liu, J., Nowaczyk, N.R., Panovska, S., Korte, M., Arz, H.W., 2020. The Norwegian-Greenland Sea, the Laschamps, and the Mono Lake Excursions Recorded in a Black Sea Sedimentary Sequence Spanning from 68.9 to 14.5 ka. Journal of Geophysical Research: Solid. Earth 125 e2019JB019225.

Liu, L., Yu, K., Li, A., Zhang, C., Wang, Le, Liu, X., Lan, J., 2023. Weathering Intensity Response to Climate Change on Decadal Scales: A Record of Rb/Sr Ratios from Chaonaqiu Lake Sediments. Western Chinese Loess Plateau, Water, p. 15.

Maldonado, A., Betancourt, J.L., Latorre, C., Villagran, C., 2005. Pollen analyses from a 50 000-yr rodent midden series in the southern Atacama Desert (25° 30′ S). J. Quat. Sci. 20, 493–507.

Mariotti, A., 1983. Atmospheric nitrogen is a reliable standard for natural 15N abundance measurements. Nature 303, 685–687.

Michalski, G., Böhlke, J.K., Thiemens, M., 2004. Long term atmospheric deposition as the source of nitrate and other salts in the Atacama Desert, Chile: New evidence from mass-independent oxygen isotopic compositions. Geochim. Cosmochim. Acta 68, 4023–4038.

Mix, A.C., Tiedemann, R., Blum, P., 2003. Proceedings of the Ocean Drilling Program Initial Reports Leg 202.

Murray, A.S., Olley, J.M., 2002. Precision and accuracy in the optically stimulated luminescence dating of sedimentary quartz: a status review. Geochronometria: Journal on Methods & Applications of Absolute Chronology 21.

Owen, J.J., Dietrich, W.E., Nishiizumi, K., Chong, G., Amundson, R., 2013. Zebra stripes in the Atacama Desert: Fossil evidence of overland flow. Geomorphology 182, 157–172.

Pavón-Carrasco, F.J., Osete, M.L., Torta, J.M., Santis, A.P.D., 2014. A geomagnetic field model for the Holocene based on archaeomagnetic and lava flow data. Earth Planet. Sci. Lett. 388, 98–109.

Pfeiffer, M., Latorre, C., Santoro, C.M., Gayo, E.M., Rojas, R., Carrevedo, M.L., McRostie, V.B., Finstad, K.M., Heimsath, A., Jungers, M.C., de Pol-Holz, R., Amundson, R., 2018. Chronology, stratigraphy and hydrological modelling of extensive wetlands and paleolakes in the hyperarid core of the Atacama Desert during the late quaternary. Quat. Sci. Rev. 197, 224–245.

Pfeiffer, M., Morgan, A., Heimsath, A., Jordan, T., Howard, A., Amundson, R., 2021. Century scale rainfall in the absolute Atacama Desert: Landscape response and implications for past and future rainfall. Quat. Sci. Rev. 254, 106797.

Placzek, C., Quade, J., Betancourt, J.L., Patchett, P.J., Rech, J.A., Latorre, C., Matmon, A., Holmgren, C., English, N.B., 2009. Climate in the dry Central Andes OVER geologic, millennial, and interannual timescales 1. Ann. Mo. Bot. Gard. 96, 386–397.

Placzek, C., Granger, D.E., Matmon, A., Quade, J., Ryb, U., 2014. Geomorphic process rates in the Central Atacama Desert, Chile: Insights from cosmogenic nuclides and implications for the onset of hyperaridity. Am. J. Sci. 314, 1462–1512.

Quade, J., Rech, J.A., Latorre, C., Betancourt, J.L., Gleeson, E., Kalin, M.T.K., 2007. Soils at the hyperarid margin: the isotopic composition of soil carbonate from the Atacama Desert, Northern Chile. Geochim. Cosmochim. Acta 71, 3772–3795.

Quade, J., Rech, J.A., Betancourt, J.L., Latorre, C., Quade, B., Rylander, K.A., Fisher, T., 2008. Paleowetlands and regional climate change in the Central Atacama Desert, northern Chile. Quat. Res. 69, 343–360.

Raisbeck, G.M., Yiou, F., 1984. Production of long-lived cosmogenic nuclei and their applications. Nucl. Inst. Methods Phys. Res. B 5, 91–99.

Ravelo, A.C., Andreasen, D.H., Lyle, M., Olivarez Lyle, A., Wara, M.W., 2004. Regional climate shifts caused by gradual global cooling in the Pliocene epoch. Nature 429, 263–267.

Rech, J.A., Currie, B.S., Michalski, G., Cowan, A.M., 2006. Neogene climate change and uplift in the Atacama Desert, Chile. Geol 34, 761–764.

Ritter, B., Binnie, S.A., Stuart, F.M., Wennrich, V., Dunai, T.J., 2018a. Evidence for multiple Plio-Pleistocene lake episodes in the hyperarid Atacama Desert. Quat. Geochronol. 44, 1–12.

Ritter, B., Stuart, F.M., Binnie, S.A., Gerdes, A., Wennrich, V., Dunai, T.J., 2018b. Neogene fluvial landscape evolution in the hyperarid core of the Atacama Desert. Sci. Rep. 8, 13952.

Ritter, B., Wennrich, V., Medialdea, A., Brill, D., King, G., Schneiderwind, S., Niemann, K., Fernández-Galego, E., Diederich, J., Rolf, C., Bao, R., Melles, M., Dunai, T.J., 2019. Climatic fluctuations in the hyperarid core of the Atacama Desert during the past 215 ka. Sci. Rep. 9, 5270.

Ruff, M., Fahrni, S., Gäggeler, H.W., Hajdas, I., Suter, M., Synal, H.-A., Szidat, S., Wacker, L., 2010. On-line Radiocarbon Measurements of Small Samples using Elemental Analyzer and MICADAS Gas Ion Source. Radiocarbon 52, 1645–1656.

Sáez, A., Godfrey, L.V., Herrera, C., Chong, G., Pueyo, J.J., 2016. Timing of wet episodes in Atacama Desert over the last 15 ka. The Groundwater Discharge Deposits (GWD) from Domeyko Range at 25°S. Quat. Sci. Rev. 145, 82–93.

Sager, C., Airo, A., Arens, F.L., Rabethge, C., Schulze-Makuch, D., 2020. New types of boulder accumulations in the hyper-arid Atacama Desert. Geomorphology 350, 106897.

Sanchez, C., Regard, V., Carretier, S., Riquelme, R., Blard, P.-H., Campos, E., Brichau, S., Lupker, M., Hérail, G., 2021. Neogene basin infilling from cosmogenic nuclides (10 be and 21 Ne) in Atacama, Chile: Implications for palaeoclimate and supergene copper mineralization. Basin Res. 33, 2549–2571.

Schulze-Makuch, D., Wagner, D., Kounaves, S.P., Mangelsdorf, K., Devine, K.G., de Vera, J.-P., Schmitt-Kopplin, P., Grossart, H.-P., Parro, V., Kaupenjohann, M., Galy, A., Schneider, B., Airo, A., Frösler, J., Davila, A.F., Arens, F.L., Cáceres, L., Cornejo, F.S., Carrizo, D., Dartnell, L., DiRuggiero, J., Flury, M., Ganzert, L., Gessner, M.O., Grathwohl, P., Guan, L., Heinz, J., Hess, M., Keppler, F., Maus, D., McKay, C.P., Meckenstock, R.U., Montgomery, W., Oberlin, E.A., Probst, A.J., Sáenz, J.S., Sattler, T., Schirmack, J., Sephton, M.A., Schloter, M., Uhl, J., Valenzuela, B., Vestergaard, G., Wörmer, L., Zamorano, P., 2018. Transitory microbial habitat in the hyperarid Atacama Desert. Proc. Natl. Acad. Sci. USA 115, 2670–2675.

Steier, P., Martschini, M., Buchriegler, J., Feige, J., Lachner, J., Merchel, S., Michlmayr, L., Priller, A., Rugel, G., Schmidt, E., others, 2019. Comparison of methods for the detection of 10Be with AMS and a new approach based on a silicon nitride foil stack. Int. J. Mass Spectrom. 444, 116175.

Stuiver, M., Reimer, P.J., 1993. Extended 14C data base and revised CALIB 3.0 14C age calibration program. Radiocarbon 35, 215–230.

Vandenberghe, J., 2013. Grain size of fine-grained windblown sediment: a powerful proxy for process identification. Earth Sci. Rev. 121, 18–30.

Vargas, G., Rutllant, J., Ortlieb, L., 2006. ENSO tropical–extratropical climate teleconnections and mechanisms for Holocene debris flows along the hyperarid coast of western South America (17°–24°S). Earth Planet. Sci. Lett. 249, 467–483.

Voigt, C., Klipsch, S., Herwartz, D., Chong, G., Staubwasser, M., 2020. The spatial distribution of soluble salts in the surface soil of the Atacama Desert and their relationship to hyperaridity. Glob. Planet. Chang. 184, 103077.

von Blanckenburg, F., Bouchez, J., Wittmann, H., 2012. Earth surface erosion and weathering from the 10Be (meteoric)/9Be ratio. Earth Planet. Sci. Lett. 351, 295–305.

Wacker, L., Fahrni, S.M., Hajdas, I., Molnár, M., Synal, H.-A., Szidat, S., Zhang, Y., 2013. A versatile gas interface for routine radiocarbon analysis with a gas ion source. Nuclear Instruments & Methods in Physics Research Section B-beam Interactions With Materials and Atoms 294, 315–319.

Wang, L., Ku, T.L., Luo, S., Southon, J.R., Kusakabe, M., 1996. 26Al-10Be systematics in deep-sea sediments. Geochim. Cosmochim. Acta 60, 109–119.

Wang, F., Michalski, G., Seo, J.-H., Granger, D.E., Lifton, N., Caffee, M., 2015. Beryllium-10 concentrations in the hyper-arid soils in the Atacama Desert, Chile: Implications for arid soil formation rates and El Niño driven changes in Pliocene precipitation. Geochim. Cosmochim. Acta 160, 227–242.

Wennrich, V., Böhm, C., Brill, D., Carballeira, R., Hoffmeister, D., Jaeschke, A., Kerber, F., Maldonado, A., May, S.M., Olivares, Lester, Opitz, S., Rethemeyer, J., Reyers, Mark, Ritter, B., Schween, J.H., Sevinç, F., Steiner, J., Walber-Hellmann, K., Melles, M., 2024. Late Pleistocene to modern precipitation changes at the Paranal clay pan, Central Atacama Desert. Glob. Planet. Chang. 233, 104349.

Willenbring, J.K., von Blanckenburg, F., 2010. Meteoric cosmogenic Beryllium-10 adsorbed to river sediment and soil: applications for Earth-surface dynamics. Earth Sci. Rev. 98, 105–122.

Wittmann, H., von Blanckenburg, F., Bouchez, J., Dannhaus, N., Naumann, R., Christl, M., Gaillardet, J., 2012. The dependence of meteoric 10Be concentrations on particle size in Amazon River bed sediment and the extraction of reactive 10Be/9Be ratios. Chem. Geol. 318, 126–138.

Wittmann, H., von Blanckenburg, F., Dannhaus, N., Bouchez, J., Gaillardet, J., Guyot, J.-L., Maurice, L., Roig, H., Filizola, N., Christl, M., 2015. A test of the cosmogenic 10Be (meteoric)/9Be proxy for simultaneously determining basin-wide erosion rates, denudation rates, and the degree of weathering in the Amazon basin. J. Geophys. Res. Earth 120, 2498–2528.